JOURNAL OF COMPUTATIONAL PHYSICS 104, 185–210 (1993)

Numerical Study of Wave Propagation on Vortex Filaments*

ANMIN QI

Department of Mathematics and Lawrence Berkeley Laboratory, University of California, Berkeley, California 94720

Received May 6, 1991; revised March 30, 1992

Simulations of a vortex tube in unbounded, inviscid, incompressible fluid flow using three-dimensional vortex filament methods are presented. The numerical parameters that determine accuracy are investigated. Methods to deal with the truncated ends, which arise in the simulation of a part of a vortex tube, are developed. The non-monotonic response of the vortex filament evolution using the vortex method to variation of core size is observed. The effect of a small torsion of a wave on vortex stretching is discussed. The long-time propagation of a periodic wave of constant helical shape along a vortex tube is illustrated.

1. INTRODUCTION

In the present paper, we study the propagation of waves along a slender "tubelike" vortex. Such wave propagation is of interest in a number of aeronautical, geophysical, and quantum mechanical phenomena [22, 25, 29]. In particular, a solitary wave propagating along a vortex filament has been observed experimentally [15, 21] and is a major component of certain quantum mechanical methods [29]. It can be demonstrated in the self-induction approximation (see below); however, it has been shown that the self-induction approximation is not a good approximation to the Euler equations [6], and solitary wave propagation contradicts our intuitive feeling about what a non-integrable system such as the Euler system in three dimensions would do.

In this paper, we shall, in particular, examine, as carefully as we can afford, the question of whether a solitary wave can propagate on a vortex filament governed by the Euler equations. This investigation requires a careful examination of the accuracy of the methods and a careful distinction between physical and spurious vortex stretching. The investigation is not definitive because of the limitations of present computing facilities, but it does confirm, to the extent that it is reliable, that a solitary wave can indeed propagate as claimed in earlier results. Various numerical questions of broader interest will be examined along the way.

The effects of numerical parameters, of the choices of core functions, and of numerical methods for solving the time evolution ordinary differential equation on the accuracy and the stability of the vortex filament methods are investigated in order to distinguish physical vortex stretching from the stretching caused by numerical factors.

A controllable single smooth initial wave on a vortex tube is important for the study of wave propagation along a vortex tube. A solitary wave solution of the localized induction approximation (LIA) meets such a requirement. We like to know whether a solitary wave, with velocity induced by the Biot–Savart law, can propagate on a vortex tube for a long time without change of its shape. If there is a stretching in a vortex tube evolution, what causes the stretching?

For convergence of the numerical scheme and for checking of the scheme's physical validity, we use several filaments to simulate a vortex tube. Some techniques to treat the truncated ends of a part of a vortex tube will also be given.

The paper is organized as follows: In Section 2, we review the physical background and the derivation of vortex filament methods. The details of the computational scheme are given. In Section 3, we study the calculation on a part of a vortex tube. The treatment at the truncated ends is given. In Section 4, we presents the numerical results with initial solitary wave data. We study the effects of the numerical methods for solving the time evolution ordinary differential equation, the core functions, core size, the time tolerance control constant, the number of filaments used to simulate a vortex tube, and the distance between filaments on the accuracy of computational results and on vortex stretching (both numerical and physical). We also study the effect of torsion of an initial solitary wave on vortex stretching. We attempt to determine how vortex stretching starts and whether a solitary wave can propagate for a long time on a vortex tube with velocity induced by the Biot–Savart law. We will show that the core size and torsion of an initial

* This work was supported in part by the Applied Mathematics Sciences subprogram of the Office of Energy Research, U. S. Department of Energy, under Contract DE-AC03-76SF-00098, and in part by the National Science Foundation under Grant DMS89-19074.

0021-9991/93 $5.00

solitary wave are the two most sensitive factors in vortex stretching. The long-time propagation of a periodic wave of constant helical shape on a vortex tube will be illustrated. The results suggest that the velocity field induced by a vortex tube governed by the Biot–Savart law can support a solitary wave propagation on the vortex tube. Finally, we discuss the invariants of the Euler equations such as total vorticity, linear impulse, and kinetic energy in the Appendix.

2. VORTEX FILAMENT METHODS

We consider unbounded, incompressible, inviscid fluid flows. The motion of such flows is described by the Euler equations

$$\frac{D\mathbf{u}}{Dt}=\frac{\partial \mathbf{u}}{\partial t}+(\mathbf{u}\cdot\nabla)\mathbf{u}=-\nabla P, \tag{1}$$

$$\nabla\cdot\mathbf{u}=0, \tag{2}$$

where $\mathbf{u}(\mathbf{x}, t)=(u, v, w)$ is the velocity field, $\mathbf{x}=(x, y, z)$ is the position, t is time, $\nabla=(\partial/\partial x, \partial/\partial y, \partial/\partial z)$ is the gradient operator, and P is pressure.

Define the vorticity $\boldsymbol{\omega}$,

$$\boldsymbol{\omega}=\nabla\times\mathbf{u}. \tag{3}$$

Taking the curl of Eq. (1), we find the *vorticity transport equation*

$$\frac{\partial\boldsymbol{\omega}}{\partial t}+(\mathbf{u}\cdot\nabla)\boldsymbol{\omega}=(\boldsymbol{\omega}\cdot\nabla)\mathbf{u}. \tag{4}$$

Vortex lines move as material lines, where a vortex line is defined as a line in the fluid whose tangent is everywhere parallel to the vorticity vector. The circulation of a vortex tube is

$$\Gamma=\oint_{C_t}\mathbf{u}\cdot d\mathbf{l}=\int_{S_t}\boldsymbol{\omega}\cdot d\mathbf{A}, \tag{5}$$

where $d\mathbf{A}=\mathbf{n}\,dA$ is an element of the open surface S_t bounded by the closed curve C_t.

The solution of equation (4) in terms of $\boldsymbol{\omega}$ is

$$\mathbf{u}=\mathscr{K}*\boldsymbol{\omega}, \tag{6}$$

where

$$\mathscr{K}(\mathbf{x})=-\frac{1}{4\pi r^3}\begin{pmatrix}0 & -z & y\\ z & 0 & -x\\ -y & x & 0\end{pmatrix}.$$

A singular filament C is a curve on which the vorticity is concentrated. We denote its circulation as Γ. The velocity induced by such a filament C is

$$\mathbf{u}(\mathbf{x}, t)=\Gamma\int_C K(\mathbf{x}-\mathbf{x}')\times d\mathbf{l}(\mathbf{x}')$$
$$=-\frac{\Gamma}{4\pi}\int_C\frac{(\mathbf{x}-\mathbf{x}')\times d\mathbf{l}(\mathbf{x}')}{|\mathbf{x}-\mathbf{x}'|^3}, \tag{7}$$

where $K(\mathbf{x})=-(1/4\pi)(\mathbf{x}/|\mathbf{x}|^3)$.

The singular part of the Biot–Savart law (Eq. (7)) can be approximated by

$$\frac{\partial\mathbf{x}}{\partial t}=\mathbf{b}\frac{\Gamma\kappa}{4\pi}\ln\frac{L}{\rho}, \tag{8}$$

where $\mathbf{b}$ is the unit binormal vector, κ is curvature, L is the length of a thin vortex tube, and ρ is the radius of cross section of the thin vortex tube. This is the self-induction approximation or LIA. Hasimoto [14] reduced the self-induction approximation (Eq. (8)) to the nonlinear Schrödinger equation and found a solitary wave solution

$$\mathbf{x}=\begin{pmatrix}s-2\dfrac{\mu}{\beta}\tanh\eta\\ 2\dfrac{\mu}{\beta}\operatorname{sech}\eta\cos\Theta\\ 2\dfrac{\mu}{\beta}\operatorname{sech}\eta\sin\Theta\end{pmatrix}, \tag{9}$$

where $\mu=1/(1+T^2)$, $\Theta=T\eta+(\beta^2-\tau^2)t$, $\eta=\beta\xi$, $T=\tau/\beta$, $\xi=s-ct$, $c=2\tau$, τ is the constant torsion, β is a constant parameter, and the variable s is arclength [2, 6, 19, 27].

Note that Eq. (7) diverges with rate $1/|\mathbf{x}-\mathbf{x}'|^2$ if $\mathbf{x}$ is a point on curve C [2]. Following Beale and Majda [5] (who have followed an idea of Hald [13] for two-dimensional vortex methods), we smooth out the singularity by replacing the kernel $\mathscr{K}$ by $\mathscr{K}_\sigma=\mathscr{K}*\psi_\sigma$, $\psi_\sigma(\mathbf{x})=\sigma^{-3}\psi(\mathbf{x}/\sigma)$, where σ is a parameter to be chosen. We assume that ψ satisfies the conditions

(i) ψ is smooth and rapidly decreasing; i.e.,

$$|D^\alpha\psi(\mathbf{x})|\leqslant C_{\alpha j}(1+|\mathbf{x}|^2)^{-j}$$

for every multi-index α and every integer j;

(ii) $\int\psi(\mathbf{x})\,d\mathbf{x}=1$

(iii) $\int\mathbf{x}^\alpha\psi(\mathbf{x})\,d\mathbf{x}=0$, $1\leqslant|\alpha|\leqslant m-1$; m is an integer.

The functions ψ_σ are called smooth delta functions because

$$\psi_\sigma(\mathbf{x})\to\delta(\mathbf{x})\qquad\text{as}\quad\sigma\to0,$$

where $\delta(\mathbf{x})$ is the Dirac function. The parameter σ is known as core size or cutoff size.

We choose K_σ as

$$K_\sigma(\mathbf{x}) = -\frac{1}{4\pi |\mathbf{x}|^3} f(|\mathbf{x}|/\sigma)\mathbf{x},$$

where function f satisfies

(1) $f(r)/r^3$ is a smooth function of r^2

(2) $f(r) \to 1$ as $r \to \infty$

(3) $\int_0^\infty f'(r)\, r^{2k}\, dr = 0$, $2 \leqslant 2k \leqslant m-2$

(4) $|D^j f(r)| \leqslant C_j r^{-l-j}$, $r \geqslant 1$, for each $j \geqslant 1$ and a fixed $l \geqslant m+1$.

The function f is called a core function or a cutoff function. The relation between f and ψ is

$$\psi = f'(r)/4\pi r^2 \tag{10}$$

(see Beale and Majda [5]).

Replace K with K_σ in Eq. (7). We find

$$\begin{aligned}\mathbf{u}_\sigma(\mathbf{x}, t) &= \Gamma \int_C K_\sigma(\mathbf{x}-\mathbf{x}') \times d\mathbf{l}(\mathbf{x}') \\ &= -\frac{\Gamma}{4\pi}\int_C f\left(\frac{|\mathbf{x}-\mathbf{x}'|}{\sigma}\right) \\ &\quad \times \frac{(\mathbf{x}-\mathbf{x}')\times d\mathbf{l}(\mathbf{x}')}{|\mathbf{x}-\mathbf{x}'|^3}.\end{aligned} \tag{11}$$

Let us consider first the evolution of an isolated thin tube of vorticity, or vortex filament, with circulation Γ. We divide this filament into segments. For the jth segment, the two ends are the points $\mathbf{x}_j$ and $\mathbf{x}_{j+1}$. Let $\delta\mathbf{l}_j = \mathbf{x}_{j+1} - \mathbf{x}_j$. Equation (11) can be written as

$$\begin{aligned}\mathbf{u}_\sigma(\mathbf{x}, t) = -\frac{\Gamma}{4\pi}\sum_{j=-\infty}^{\infty}\int_{\delta\mathbf{l}_j} \frac{(\mathbf{x}-\mathbf{x}')\times d\mathbf{l}(\mathbf{x}')}{|\mathbf{x}-\mathbf{x}'|^3} \\ \times f\left(\frac{|\mathbf{x}-\mathbf{x}'|}{\sigma}\right).\end{aligned} \tag{12}$$

We require $|\delta\mathbf{l}_j| \leqslant h$ for all j, where h is a predetermined small number. Thus

$$\begin{aligned}\int_{\delta\mathbf{l}_j} \frac{(\mathbf{x}-\mathbf{x}')\times d\mathbf{l}(\mathbf{x}')}{|\mathbf{x}-\mathbf{x}'|^3} f\left(\frac{|\mathbf{x}-\mathbf{x}'|}{\sigma}\right) \\ \approx \frac{\mathbf{r}_j \times \delta\mathbf{l}_j}{r_j^3} f\left(\frac{r_j}{\sigma}\right),\end{aligned} \tag{13}$$

where

$$\mathbf{r}_j = \mathbf{x} - \tfrac{1}{2}(\mathbf{x}_{j+1} + \mathbf{x}_j)$$

$$r_j = |\mathbf{r}_j|.$$

Inserting Eq. (13) into Eq. (12) and replacing ∞ with a large integer N if the filament is infinitely long, we have

$$\mathbf{u}_\sigma(\mathbf{x}, t) = -\frac{\Gamma}{4\pi}\sum_{j=-N}^{N} \frac{\mathbf{r}_j \times \delta\mathbf{l}_j}{r_j^3} f\left(\frac{r_j}{\sigma}\right). \tag{14}$$

Note that for an infinitely long vortex filament, we actually compute a finite part of the filament.

Knowing $\mathbf{u}_\sigma$, we solve the ordinary differential equations

$$\frac{d\mathbf{x}}{dt} = \mathbf{u}_\sigma(\mathbf{x}, t) \tag{15}$$

and we can determine the position of $\mathbf{x}_j$ at the next time $t + \Delta t$. There are various numerical methods for solving Eq. (15); we have used the first-order Euler method, the second-order Heun method, and the fourth-order Runge–Kutta method.

A filament may stretch as the flow evolves; thus $\delta\mathbf{l}_j$ and the amount of vorticity carried by this vortex element grow. If $|\delta\mathbf{l}_j| > h$, we split this segment in two at the middle of $\delta\mathbf{l}_j$, with lengths $|\delta\mathbf{l}_j|/2$, to maintain the partition fine enough for accurate computation.

We also need to control our time tolerance Δt. The requirement for the choice of Δt at step n is given by

$$\Delta t^n \max_j |\mathbf{u}_j^n| \leqslant C, \tag{16}$$

where C is a given constant, $\mathbf{u}_j^n = \mathbf{u}_\sigma(\mathbf{x}_j(t^n), t^n)$, and t^n is the time at step n.

From the accuracy of the scheme, we require $\sigma = h^q$, $0 < q < 1$, or simply $\sigma/h > 1$ [1, 3, 4, 12]. For the scheme given above, we take the cutoff parameter σ as constant for the whole filament. The vorticity distribution can be computed by

$$\boldsymbol{\omega}_\sigma(\mathbf{x}, t) = \Gamma \sum_j \psi_\sigma(\mathbf{r}_j(t))\, \delta\mathbf{l}_j(t). \tag{17}$$

We have completed the description of the vortex filament methods for an isolated thin filament. We must use several filaments to simulate a vortex tube. The cross section of a real vortex filament or tube should be allowed to deform as the flow evolves, and the deformation may be seen by using several filaments to simulate a vortex tube [17, 31–33].

For several filaments, e.g., M filaments, we can modify Eq. (11) as follows:

$$\mathbf{u}_\sigma(\mathbf{x}, t) = \sum_{m=1}^{M} \Gamma^{(m)} \int_{C_m} K_{\sigma_m}(\mathbf{x}(t) - \mathbf{x}'(t))\, d\mathbf{l}(t).$$

Note that the circulation and core size may not be chosen to be the same value for all filaments. Equation (14) can be modified as

$$\mathbf{u}_\sigma(\mathbf{x}, t) = -\frac{1}{4\pi} \sum_{m=1}^{M} \Gamma^{(m)} \times \sum_{j=-N_m}^{N_m} \frac{\mathbf{r}_j^{(m)} \times \delta\mathbf{l}_j^{(m)}}{(r_j^{(m)})^3} f\left(\frac{r_j^{(m)}}{\sigma}\right), \tag{18}$$

where $\sigma = \sigma_m$ if $\mathbf{x}$ is not on any given filament and $\sigma = ((\sigma_m^2 + \sigma_l^2)/2)^{1/2}$ or $\sigma = (\sigma_m \sigma_l)^{1/2}$ if $\mathbf{x}$ is on the lth filament.

σ_m may also be varied with time or with arc length to conserve volume. However, with varying core size, we are not able to produce any meaningful results except for the fast stretching at a few perturbed regions which terminates all of our computations within a hundred computational steps. At this stage, it is not clear why varying core size cannot produce a satisfactory result with the method described above. For this reason, we only consider constant core size through this paper.

3. CALCULATIONS ON PART OF A VORTEX TUBE

It is often convenient to calculate part of a (possibly infinitely long) vortex tube. To do this, we must truncate the tails of a vortex tube. Consider first a straight vortex tube. Assume that the tube consists of a bundle of straight parallel filaments with equal circulation. To simplify the discussion, we assume that the straight filaments are parallel to the x-axis. Denote a plane parallel to the y-z plane and passing through the point $(x, 0, 0)$ on the x-axis by P_x. Thus P_0 is the y-z plane. We define the velocity pole $C_v(x)$ on the plane P_x as the point where the y-z component of velocity is zero. There may be several poles for a velocity field. For simplicity, we consider only the pattern of the velocity distribution with one pole on a given plane P_x. Let C_v be a curve consisting of all $C_v(x)$.

The filaments away from the pole curve C_v will rotate around the C_v. The rotation speed at different point (x, y, z) changes according to the values of the y and z coordinates. For an infinitely long straight vortex tube, the velocity distribution on the plane P_x should be the same for different x. Thus, all points on the same straight filament should rotate with the same speed around the velocity pole curve C_v. Without proper treatment at the truncated ends, a computational result of part of a vortex tube will not preserve the above property due to the loss of the appropriate contribution from the truncated parts during the computation. Near the truncated ends, the computed velocity magnitude will be quite different from the velocity magnitude induced by the whole vortex tube. Consequently, the points on the same straight filament will rotate with different speeds. A physically unreasonable twisting of filaments will start at the truncated ends and quickly spread to the middle.

The way we choose to eliminate this physically unreasonable twisting of filaments is to recover the correct velocity intensity near the truncated ends. To do this, we assume that either the data is periodic, or there is no disturbance for the place far away from the center of computed part. In the first case, we copy the computed part at each end and connect it to the previous part. In the second case, for each filament, at each end, we copy the end segment $2N_m + 1$ times and connect them to each other at the end. We call the treatment for the second case the straight line extension. For the treatments of both cases, the three-dimensional vortex filament method scheme (Eq. (18)) can be modified as

$$\mathbf{u}_\sigma(\mathbf{x}, t) = -\frac{1}{4\pi} \sum_{m=1}^{M} \Gamma^{(m)} \times \sum_{j=-N_m}^{N_m} \left[\frac{\mathbf{r}_j^{(m)} \times \delta\mathbf{l}_j^{(m)}}{(r_j^{(m)})^3} f\left(\frac{r_j^{(m)}}{\sigma}\right) + \frac{\tilde{\mathbf{r}}_j^{(m)} \times \delta\mathbf{l}_j^{(m)}}{(\tilde{r}_j^{(m)})^3} f\left(\frac{\tilde{r}_j^{(m)}}{\sigma}\right) + \frac{\bar{\mathbf{r}}_j^{(m)} \times \delta\mathbf{l}_j^{(m)}}{(\bar{r}_j^{(m)})^3} f\left(\frac{\bar{r}_j^{(m)}}{\sigma}\right) \right],$$

where

$$\mathbf{r}_j = \mathbf{x} - \tfrac{1}{2}(\mathbf{x}_{j+1} + \mathbf{x}_j)$$
$$\tilde{\mathbf{r}}_j = \mathbf{x} - \tfrac{1}{2}(\tilde{\mathbf{x}}_{j+1} + \tilde{\mathbf{x}}_j)$$
$$\bar{\mathbf{r}}_j = \mathbf{x} - \tfrac{1}{2}(\bar{\mathbf{x}}_{j+1} + \bar{\mathbf{x}}_j)$$
$$r_j = |\mathbf{r}_j|$$
$$\tilde{r}_j = |\tilde{\mathbf{r}}_j|$$
$$\bar{r}_j = |\bar{\mathbf{r}}_j|.$$

For the periodic data,

$$\tilde{\mathbf{x}}_j = \begin{pmatrix} x_{N_m+1} + x_j - x_{-N_m} \\ y_j \\ z_j \end{pmatrix},$$

$$\bar{\mathbf{x}}_j = \begin{pmatrix} x_{-N_m} - (x_{N_m+1} - x_j) \\ y_j \\ z_j \end{pmatrix}.$$

For the straight line extension,

$$\tilde{\mathbf{x}}_j = \begin{pmatrix} 2\tilde{x}_{j-1} - \tilde{x}_{j-2} \\ y_{N_m+1} \\ z_{N_m+1} \end{pmatrix},$$

$$\bar{\mathbf{x}}_j = \begin{pmatrix} 2\bar{x}_{j-1} - \bar{x}_{j-2} \\ y_{N_m+1} \\ z_{N_m+1} \end{pmatrix},$$

where $\tilde{x}_{-N_m} = x_{N_m+1}$, $\tilde{x}_2 = 2x_{N_m+1} - x_{N_m}$, $\bar{x}_{-N_m} = x_{-N_m}$, and $\bar{x}_{-N_m+1} = 2x_{-N_m} - x_{-N_m+1}$. One should modify the scheme of straightline extension to deal with the situation of perturbed waves passing through the truncated ends.

4. NUMERICAL RESULTS

4.1. *Goal and Experimental Design*

We present our numerical results in this section. Our goal is to answer the following questions:

A. What are the effects of the choices of the numerical methods for solving the time evolution ordinary differential equation, the core functions, and the parameters on the accuracy of our vortex filament scheme?

B. What are the main factors causing numerical and physical vortex stretching?

Solitary wave propagation along a vortex tube is the physical-model problem we study here to provide answers for the above questions. Besides, solitary wave propagation along a vortex tube is an interesting research subject in itself. In particular, we would like also to know

C. Can a solitary wave propagate along a vortex tube for a long time?

The numerical and physical factors we are going to examine are the following:

1. the numerical method we choose to solve the time evolution ordinary differential equation;
2. the core function we construct to approximate the singular Biot–Savart kernel;
3. the core size σ defined in Section 2;
4. the time tolerance control constant C;
5. the number of filaments used to simulate a vortex tube;
6. the distance between filaments;
7. the circulation Γ defined in Eq. (5); and
8. the torsion τ of the initial solitary wave data generated by Eq. (9).

In the list, the numerical method solving the time evolution ordinary differential equation, the core function, the time tolerance control constant C, and the number of filaments used in the simulation of a vortex tube are clearly numerical factors. The accuracy of our results and the efficiency of our computation depend on these factors. The circulation Γ and the torsion τ of the initial solitary wave data are physical factors chosen in accordance with the physical phenomenon we attempt to simulate. The core size and the distance between filaments could have both numerical and physical significance, which we will explain later in this section.

To answer question A, we must examine the sensitivity of our numerical algorithm to the factors 1–8 listed above. In a computational result, a vortex tube stretching can be caused by either the computational inaccuracy or physical nature, or both. We will try to distinguish the different causes of the vortex stretching appearing in our results whenever it is possible. The answers to questions A to B will help us to answer question C.

In our vortex filament method, we split a segment two if the length of this segment is larger than a predetermined positive number. When a filament starts stretching, the total arclength of the filament will grow very quickly. Thus, the number of segments needet of vortex stretching. The total arclength is proportional to the total number of segments.

Both numerical inaccuracy and the physical nature of the vorticity field can cause vortex stretching. The numerical errors often introduce high-frequency perturbation waves with small torsion. Such waves easily cause violent stretching, as we will explain later. This type of stretching is numerical stretching. Chorin [11] has given a statistical analysis according to which there is an upper bound on the possible folding of a vortex line in inviscid flow (measured by its fractal dimension); he also showed that if a vortex line is discretized and, in particular if its smallest scales are not well resolved, that physical bound can be crossed and a discrete vortex line will fold more than the continuum Euler equations can allow. Thus it is a virtue of vortex methods that they allow vortex stretching and folding, but this virtue can become a flaw if the stretching is allowed to cross the physical bound. The difference between physical and numerical stretching is difficult to determine; presumably, as long as the physical invariants are well approximated, the stretching is physical. We can also look at the geometric pattern of a perturbation wave and the location of the appearance of the wave to decide whether the perturbation wave is caused by numerical error or by physical instability and thus distinguish physical stretching from numerical stretching.

Computer memory limits the maximum number of segments per filament. If the number of segments for any filament exceeds the maximum value, our computation is stopped at that step. Thus, the smaller the number of steps for which our computation can be carried out, the more

stretching we obtain for the simulated vortex tube. If a computation can be carried out till the allowed maximum step, then the total number of segments at that step reflects the stretching of the simulated vortex tube; the larger the number of total segments implies more stretching in the computation.

We define an elapsed time of a computation as an accumulated sum of the time tolerances for each computational step from the beginning to the last step. The elapsed time is an indicator of the efficiency of our computation and a diagnostic of the accuracy of the computational results, because the slower growth of the elapsed time usually means that the time tolerance of each step is too small and thus may be not efficient. The rapid growth of the elapsed time means that the time tolerance of each step is large and may therefore cause inaccuracy.

The kinetic energy, total vorticity, and linear impulse are conserved quantities on whole vorticity field for the Euler equations. Thus, on the whole vorticity field, a variation from the initial value of each of these quantities indicates error. However, in the computation of a portion of a vortex tube, the case in which we are interested for all computations shown in this section, the kinetic energy of the portion is approximately conserved only if perturbation waves are far from the truncated ends, and linear impulse is not conserved at all as long as there are perturbations in the computed portion of a vortex tube. The total vorticity is conserved in all cases. Therefore, a variation from the initial value of the total vorticity indicates error. If the computed kinetic energy is conserved, our computational results may be accurate, but a variation of the computed kinetic energy of the portion of a vortex tube does not necessarily mean that the result is bad (inaccurate). We should not use linear impulse as a diagnostic of our numerical schemes in this paper. One should refer to the Appendix for detailed analysis. Therefore, we use the following quantities to measure the accuracy and the vortex stretching of our computational results:

1. the number of steps carried out in a computation;
2. the number of segments at the last computational step;
3. the total arclength at the last computational step;
4. the elapsed time;
5. the total vorticity of the computer part; and
6. the total kinetic energy of the computed part.

In each numerical experiment, we generate initial vortex filament curves from Eq. (9) with predetermined parameters. Each curve approaches at infinity a line parallel to the x-axis. Therefore, we should see the initial wave in each filament propagating along the x-axis. There are three parameters that may change the shape of the initial curve: (1) the torsion τ, (2) the parameter β, and (3) the initial time parameter t_0, which merely determines the position of the initial wave. The $|\beta|$ determines the amplitude of curvature κ, and increasing $|\tau|$ will increase the speed of the wave and decrease the amplitude of the wave [27]. In our computation, we record the measurements described above and the propagation behavior of the initial wave for various combinations of the investigated factors. We will use tables or figures to display the results in terms of those measurements. Finally, we will analyze the results obtained and try to find answers for our questions.

4.2. *Numerical Factors*

We start the discussion with number of filaments used to simulate a vortex tube. To understand a wave motion in an inviscid incompressible fluid flow, we would like to determine the propagation behavior of the initial wave in the velocity field induced by a thin vortex tube governed by the Biot–Savart law. A single filament can be viewed as a thin vortex tube. However, the lack of change of core structure in the cross section of a filament makes the simulation of a thin vortex tube by a single filament physically unreasonable, because the shape of a vortex tube core is not preserved [17, 23, 24, 26]. Moreover, for a "fat" vortex tube, it is unreasonable to approximate the tube by one filament with large core size because, mathematically, it is unreasonable to approximate the singular kernel $K(\mathbf{x})$ given in Section 2 by the smoothed kernel $K_\sigma(\mathbf{x})$ with large σ—the core size. Note that when we increase the number of filaments, we should decrease the circulation of each filament to preserve the total circulation of the simulated vortex tube. Nevertheless, the one filament simulation of a thin vortex tube gives us some useful information on vortex stretching and how vortex filament methods respond to various parameters.

Theoretically, the accuracy will increase as a vortex tube is simulated with an increasing number of filaments. However, the simulations of our physical-model problem require long filaments and, therefore, many segments for each filament and long time computations to obtain enough information to understand the questions raised at beginning of this section. The cost of the computation and the capacity of computer memories do not permit us to simulate a vortex tube with many filaments. We will provide results of one-filament simulations and of four-filament simulations for some of the following computational experiments.

In this subsection, all initial data of our computation are generated from Eq. (9) with $\tau = 3.0$, $\beta = 2.0$. The length ds of each segment is 0.04 initially. A segment must split in two of its length is longer than 0.05, i.e., $h = 0.05$. The computation is terminated if there is a filament with more than 1000 segments.

We examine the following numerical methods for solving the time evolution ordinary differential equation—the

numerical ODE solvers: (1) the first-order Euler method, (2) the second-order modified trapezoidal method (the second-order Heun method), and (3) the fourth-order Runge–Kutta method (RK4). The core functions we examined are the following:

$$\text{Core 1: } 1-e^{-r^3};$$

$$\text{Core 2: } \tanh r^3;$$

$$\text{Core 3: } 1+(-1+\tfrac{3}{2}r^3)\,e^{-r^3};$$

$$\text{Core 4: } \tanh r^3+\tfrac{3}{2}r^3\,\operatorname{sech}^2 r^3.$$

We make runs with each numerical ODE solver and each core function for one filament and for four filaments. In Table I, we list the total number of computational steps, the total number of segments at the last computational step, the total arclength at the last computational step, and the elapsed time.

From Table I we see that with the first-order Euler method, the rate of stretching is much faster than the rate of stretching with other two methods. We believe that the fast stretching rate is largely due to numerical error because most of stretching is caused by high frequency waves which occurred where no such waves had been observed using other higher order ODE solvers. Therefore, we think that the results produced with the first-order Euler method is much less accurate than the results produced with other two ODE solvers and did not make runs for four filaments with the Euler method. There is no great difference for the results made with the second-order modified trapezoidal method and the results made with the fourth-order Runge–Kutta method. We will use the fourth-order Runge–Kutta method for the rest of our runs in this section.

TABLE I

Comparisons of the Total Number of Computational Steps Performed, the Total Number of Segments (N) at the Last Computational Step, the Total Arclength (s) at the Last Computational Step, and the Elapsed Time (T) for Various Core Functions and Numerical ODE Solvers with One Filament and with Four Filaments

		One filament				Four filaments		
			At last step			At step 200		
Methods	Core	Steps	N	T	s	N	T	s
Euler	1	104	993	1.410	34.95	—	—	—
	2	84	982	1.255	34.84	—	—	—
	3	78	993	0.755	35.07	—	—	—
	4	84	991	0.665	35.18	—	—	—
Heun	1	139	974	1.980	33.69	2258	2.050	77.66
	2	140	986	1.940	34.28	2369	2.020	82.84
	3	200	510	1.945	17.80	1867	1.155	64.66
	4	200	529	1.815	18.67	1815	1.045	64.42
RK4	1	142	977	2.010	33.86	2332	2.050	80.91
	2	145	982	1.990	33.99	2506	2.020	87.34
	3	200	558	1.985	20.28	1848	1.185	64.72
	4	200	510	1.925	16.74	1798	1.075	64.38

Note. These calculations were performed with the periodic data assumption and with parameters of core size $\sigma=0.2$, $t_0=-0.1$, $C=0.05$, $\tau=3.0$, and $\beta=2.0$. $\Gamma=5.0$ for one filament simulation. For four filament simulations, $\Gamma=1.25$; the initial distance between filaments was 0.05.

Table I shows that use of different core functions produces different results. We cannot really see, however, which core function gives us a more accurate solution because the behavior of a core function is governed by the core size. Each core function responds to a same value of core size differently.

We calculated the kinetic energy of the particular part of vortex tube by use of the scheme (27) in the Appendix, where the ∞ is replaced by N_m—the number of segments for the mth filament. For the reason explained at the end of the Appendix and at the end of Section 4.1 the computed value of kinetic energy is, at best, approximately conserved. In Table II, we displayed the variations of total vorticity and kinetic energy of the computed portion of a vortex tube. The data shown in Table II are calculated according to the following formulations:

K.E. (%). the percentage of maximum variation of kinetic energy from the initial kinetic energy is

$$\frac{\left(\max_n |\text{kinetic energy at step } n\right.\\ \left.-\text{initial kinetic energy}|\right)}{\text{initial kinetic energy}}\times 100;$$

T.Vor. (%). the percentage of maximum variation of total vorticity from the initial total vorticity is

$$\frac{\left(\max_n \|\text{total vorticity at step } n\right.\\ \left.-\text{initial total vorticity}\|\right)}{\|\text{initial total vorticity}\|}\times 100.$$

From Table II, we can see that the total vorticity is well conserved for all cases, and the computed kinetic energy has some variations as we expected from the analysis in the Appendix. We also illustrated the behaviors of total vorticity and kinetic energy in the computation in Fig. 1. From both Table II and Fig. 1 we can see that the four-filament simulations give better results in terms of the diagnostics—total vorticity and kinetic energy. From Fig. 1, for the computations using the second-order modified trapezoidal method and the fourth-order Runge–Kutta method, the order of core function and the order of the numerical ODE solver have a visible effect on the computed

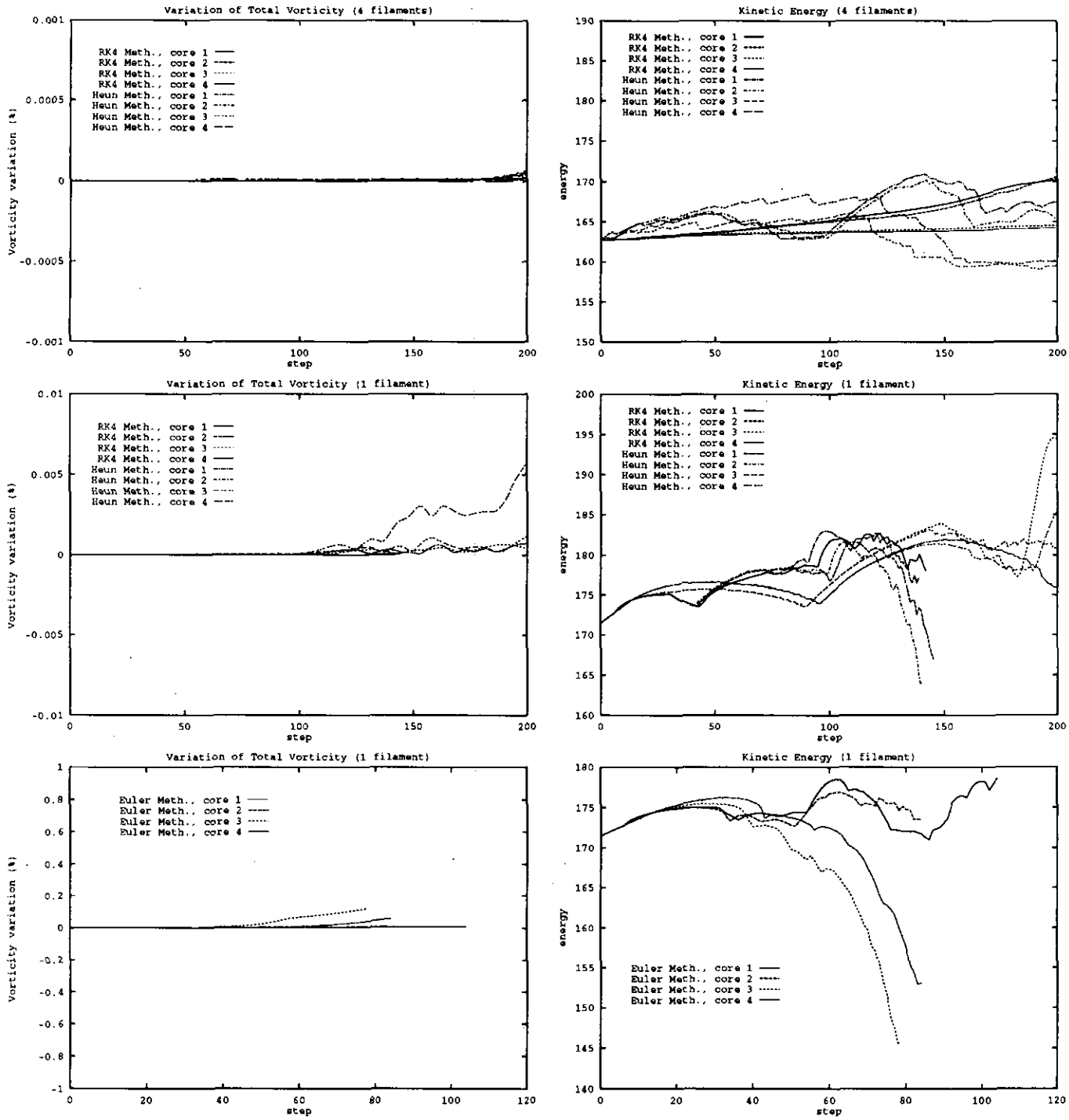

FIG. 1. The diagnostics of computation for various ODE solvers and core functions.

kinetic energy. According to Beale and Majda [5], core function 1 and core function 2 are of second order, and core function 3 and core function 4 are of fourth order.

From Eq. (16),

$$\Delta t^n \max_j |\mathbf{u}_j^n| \leqslant C.$$

The time tolerance control constant C is one of the factors determining the accuracy of our computational results. However, if C is too small, the computational cost will be quite high. In Table III we see that when we increase C, the elapsed time, the number of segments, and the arclength at the last computational step are increased, and the number

TABLE II

The Percentages of Maximum Variation of Kinetic Energy from the Initial Kinetic Energy and of Maximum Variation of Total Vorticity from the Initial Total Vorticity in the Computed Portion

ODE solver	Core	One filament		Four filaments	
		K.E. (%)	T. Vor. (%)	K.E. (%)	T. Vor. (%)
Euler	1	4.135	0.008606	—	—
	2	3.178	0.007783	—	—
	3	15.19	0.120818	—	—
	4	10.81	0.058267	—	—
Heun	1	6.706	0.000025	5.011	0.000065
	2	5.871	0.000071	4.550	0.000018
	3	6.816	0.001153	2.315	0.000059
	4	8.095	0.005762	3.478	0.000018
RK4	1	6.531	0.000022	4.652	0.000018
	2	5.923	0.000102	4.820	0.000018
	3	13.45	0.000671	1.128	0.000043
	4	6.104	0.000720	0.930	0.000018

Note. See Table I for the choices of parameters.

of computational steps needed to reach a given value of elapsed time is decreased. In Table III, for $C \geq 0.06$, we see the dramatic increase in the number of segments and the arclength at the last computational step and the decrease of the number of computational steps needed to reach the elapsed time 0.1575. Such dramatic changes indicate that the computational results with the parameters given at the footnote of Table III are not accurate for $C > 0.05$.

The choice of C depends on the maximum amplitude of the velocity induced by the filaments and therefore depends on the circulation Γ. From Eq. (18), increasing Γ will increase the amplitude of velocity, whereas, from Eq. (16), increasing the amplitude of the velocity for a given constant C will decrease the time-step tolerance Δt. However, in two runs, if the only difference is the constant circulation number, say $\Gamma_1 \neq \Gamma_2$, and the equation

$$\Delta t^n \max_j |\mathbf{u}_j^n| = C \tag{19}$$

is used to determine Δt^n at each step instead of Eq. (16) for both runs, then the stretching behavior of filaments for the two runs will be identical. The reason is that if $\Gamma_1^{(m)} = \Gamma_1$ and $\Gamma_2^{(m)} = \Gamma_2$ for $m = 1, \ldots, M$ in two runs, and if at step n and each space point x_j,

$$\frac{u_i^1(x_j, t^n)}{u_i^2(x_j, t^n)} = \frac{\Gamma_1}{\Gamma_2}, \qquad i = 1, 2, 3, \tag{20}$$

where $(u_1, u_2, u_3) = (u, v, w) = \mathbf{u}$, then

$$\Delta t_1^n \Gamma_1 = \Delta t_2^n \Gamma_2$$

if Eq. (19) is used to determine Δt_1^n and Δt_2^n; thus each space point x_j on a filament will evolve the same for both runs, and equality (20) will remain at next step.

4.3. *Core Size*

As discussed in Subsection 4.2, the core size should not be too large because of the mathematical unreasonableness to approximate the singular kernel $K(\mathbf{x})$ by $K_\sigma(\mathbf{x})$ with large core size σ. The core size is an important numerical factor. However, we could think of core size as the thickness of our filaments; thus the core size could have some physical significance for a thin vortex filament. We would like to find a reasonable range of core sizes and the responses of our computational results to the choices of various core sizes.

In Table IV and Table V, we displayed the results of the total number of computational steps, the number of total segments at the last computational step, the elapsed time, and the total arclength at the last compuational step for runs made with various core sizes. The maximum number of

TABLE III

Comparisons of the Total Number of Computational Steps Performed, the Total Number of Segments (N) at the Last Computational Step, the Total Arclength (s) at the Last Computational Step, and the Elapsed Time (T) for Various Time Tolerance Control Constants C

C	Steps	At the last step		
		N	T	s
0.02	250	1709	0.15750	64.04793
0.03	250	1778	0.24875	64.27265
0.04	250	1879	0.31375	65.23524
0.05	250	1934	0.33125	66.26626
0.06	250	3518	0.43500	119.03595
0.07	175	3624	0.43500	122.79700
0.10	162	3647	0.42500	124.47843

Steps needed to reach the elapsed time 0.1575

C	Steps	At the last step		
		N	T	s
0.02	250	1709	0.15750	64.04793
0.03	132	1710	0.15750	64.04794
0.04	125	1709	0.15750	64.04791
0.05	111	1710	0.15750	64.04775
0.06	65	1710	0.15625	64.04724
0.07	63	1710	0.15750	64.04726
0.10	55	1713	0.15750	64.04207

Note. These calculations were performed for four filaments using the fourth-order Runge–Kutta method and the core function 4 with the periodic data assumption and with parameters of core size $\sigma = 0.2$, $t_0 = -0.2$, $\Gamma = 5.0$, $\tau = 3.0$, and $\beta = 2.0$. The initial distance between filaments was 0.05.

computational steps is 250 for each run. The maximum number of segments for each filament is 1000. Therefore, if a run is stopped before the 250th step, it indicates that a violent stretching occurred. The fewer the total steps for a run, the sooner a violent stretching occurs. If a run is stopped at step 250, the total number of segments measures the intensity of stretching in that run. The vortex stretching phenomenon can be better illustrated by figures (see Fig. 2 for the one-filament simulation).

It is interesting to see from Tables IV and V that the rate of stretching does not respond monotonically to the core size. Such a phenomenon is shown directly in terms of arclength in Table IV for runs made with a single filament and with core function 4 and in Table V for runs made with four filaments. Krasny [18] has reported the nonmonotonical response to core sizes for a two-dimensional blob method with a core structure different from those used here. We observed from Table IV and Table V that choosing core size at a certain range, we can obtain a very low rate of stretching. The range is around 0.1 and 0.55 in Table IV for core function 4 and around 0.2 and 0.6 in Table V.

In Table IV, the values of arclength are close to each other for those runs terminated before the 250th step. From this observation, we conclude that the number of segments grows rapidly once stretching starts in a run. From both Tables IV and V, we see that the total elapsed time increases when we increase the core size. It means that the time tolerance Δt for each step determined by Eq. (16) is larger

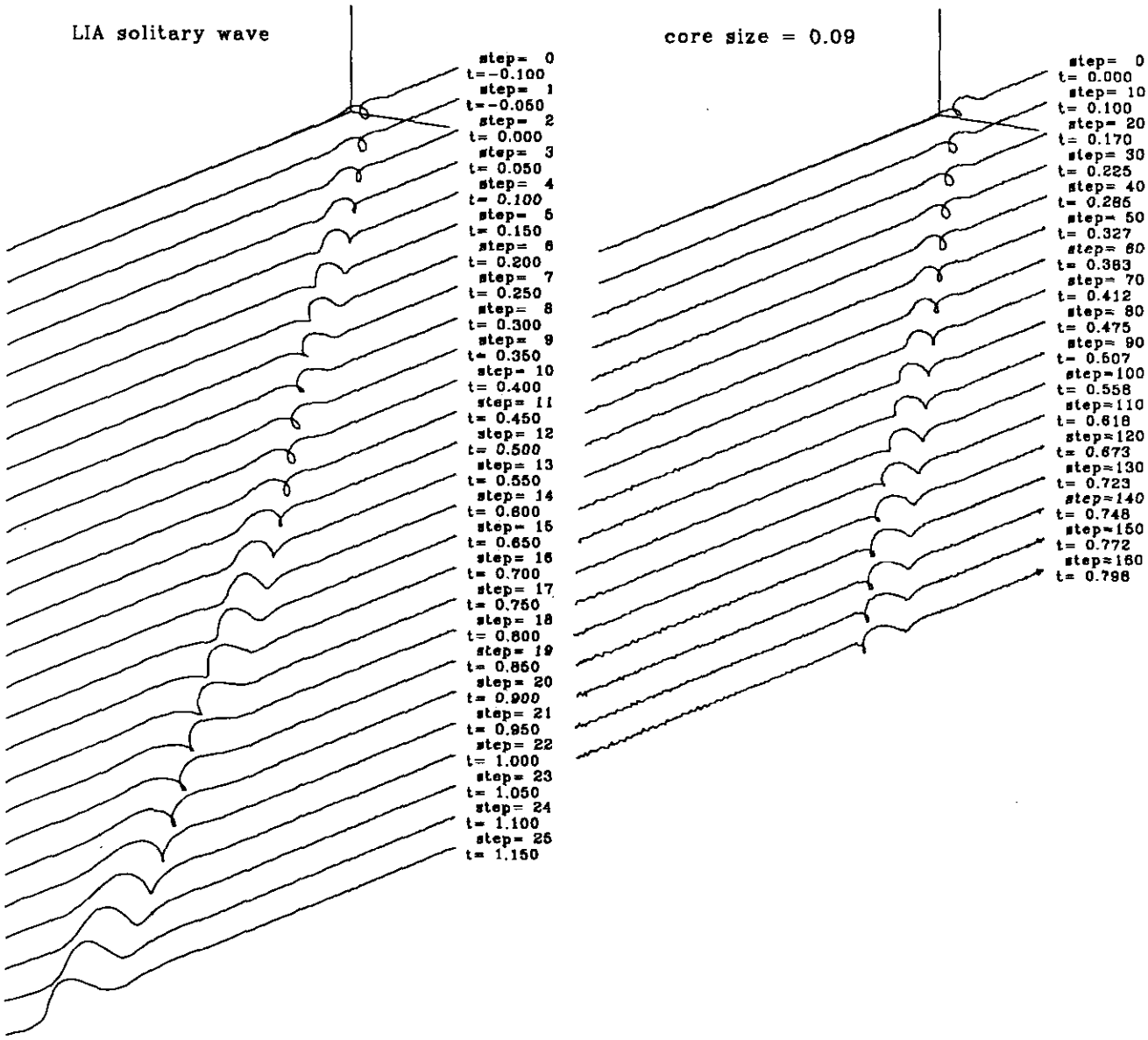

FIG. 2. Perspective views of wave propagating on one filament for various core size.

for larger core size; that is, the maximum amplitude of the velocity increases when we increase the core size.

Figure 2 shows the geometric shapes of waves propagating on one filament for various core sizes. The data correspond to the results in Table IV with core function 4. In all the runs, the initial wave can propagate without significantly changing shape for certain computational steps; then, the wave either splits into several waves or starts to stretch with different geometric shapes, depending on the core size and other parameters. For smaller core sizes, the propagation of the initial wave is closer to the analytic solution of LIA in terms of the phase of the wave.

The following are the summary of our observation made from Fig. 2:

• For core size equal to 0.55, we see a smaller wave split from the original one with a stable shape propagating in the positive direction on the x-axis. Later, several waves split and move away from the original wave. When the core size is 0.35, stretching happens soon after some perturbation appears in front of the initial wave. A similar phenomenon occurs for the run made with core size $\sigma = 0.2$, but the geometric structure of the stretching is quite different.

• All stretching happens in a narrow region in the x-direction; that is, the stretching does not spread along the x-direction.

• In the case of core size $\sigma = 0.2$, a long arm comes out from the filament and wraps around the axis on which the

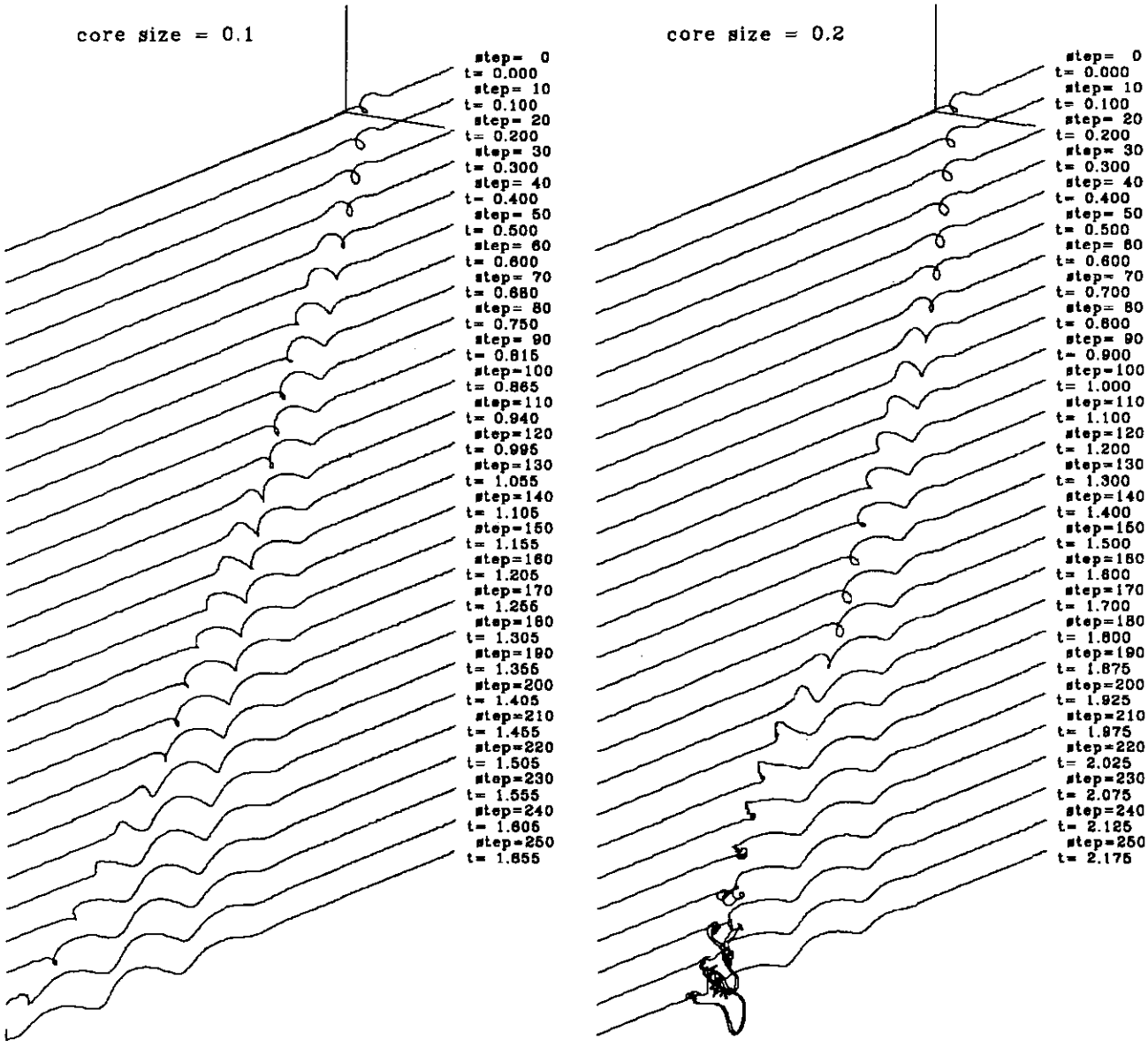

FIG. 2—*Continued*

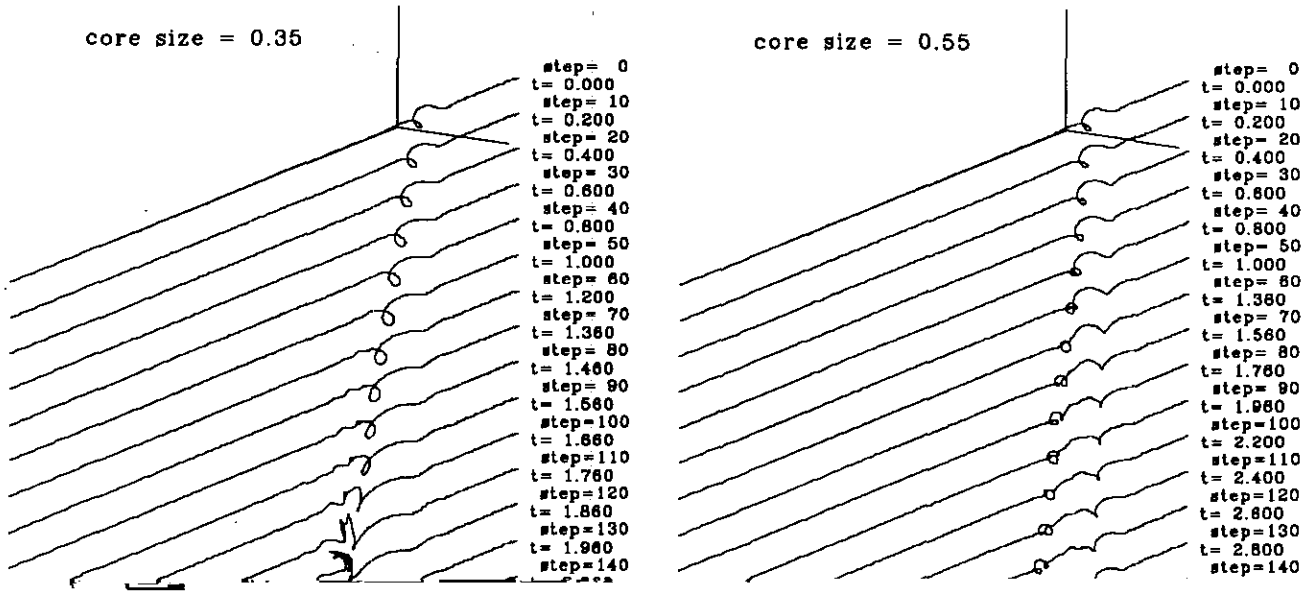
core size = 0.35
step= 0
t= 0.000
step= 10
t= 0.200
step= 20
t= 0.400
step= 30
t= 0.600
step= 40
t= 0.800
step= 50
t= 1.000
step= 60
t= 1.200
step= 70
t= 1.360
step= 80
t= 1.460
step= 90
t= 1.560
step=100
t= 1.660
step=110
t= 1.760
step=120
t= 1.860
step=130
t= 1.960
step=140
core size = 0.55
step= 0
t= 0.000
step= 10
t= 0.200
step= 20
t= 0.400
step= 30
t= 0.600
step= 40
t= 0.800
step= 50
t= 1.000
step= 60
t= 1.360
step= 70
t= 1.560
step= 80
t= 1.760
step= 90
t= 1.960
step=100
t= 2.200
step=110
t= 2.400
step=120
t= 2.600
step=130
t= 2.800
step=140

TABLE IV

Comparisons of the Total Number of Computational Steps Performed, the Total Number of Segments (N) at the Last Computational Step, the Total Arclength (s) at the Last Computational Step, and the Elapsed Time (T) for Various Core Sizes and for Two Types of Core Functions with One Filament

Core functions	Core size	Steps	At the last step		
			N	T	s
Core 1	0.05	88	878	0.3975	31.29
	0.08	237	963	1.785	34.16
	0.09	238	978	1.9025	33.67
	0.095	241	983	1.945	33.78
	0.10	240	972	1.975	33.34
	0.11	234	987	2.025	34.03
	0.15	193	979	2.03	34.50
	0.20	142	977	2.01	33.86
	0.25	146	993	2.22	34.41
	0.30	218	992	4.04	33.21
	0.35	250	636	5.34	19.03
	0.40	250	602	6.64	17.00
Core 4	0.05	61	953	0.14063	33.90
	0.08	51	948	0.1725	33.27
	0.09	168	980	0.8175	32.02
	0.10	250	502	1.655	16.52
	0.15	250	512	1.99	16.70
	0.20	250	813	2.18	28.18
	0.25	213	991	2.16	34.12
	0.30	157	993	2.09	34.51
	0.35	149	982	2.15	34.09
	0.40	237	997	3.29	33.05
	0.45	250	685	4.23	21.47
	0.50	250	602	5.00	16.83
	0.55	250	575	5.20	16.56
	0.60	250	695	10.00	16.64

Note. These calculations were performed for one filament using the fourth-order Runge–Kutta method with the periodic data assumption and with parameters $t_0 = -0.2$, $C = 0.05$, $\Gamma = 5.0$, $\tau = 3.0$, and $\beta = 2.0$.

In conclusion, we should not choose core size too big, say bigger than 1, or smaller than 0.1 if we use single precision in computation. In the range [0.1, 1], the vortex filaments will behave differently for different choices of core size. It is possible to obtain a long time stable (less stretching) result of a wave propagating on filaments for certain choices of core size. We have not found a proper analytic method to determine that value. The choice of core size, now, very much depends on experience and experimental observation.

4.4. *Factors Affecting the Placement of Filaments*

The different choices of initial distance between filaments (in multi-filament simulations) could produce different velocity distribution, as illustrated in Fig. 3 and in Fig. 4 for four filaments. Evidently, the choice of the initial distance

TABLE V

Comparisons of the Total Number of Computational Steps Performed, the Total Number of Segments (N) at the Last Computational Step, the Total Arclength (s) at the Last Computational Step, and the Elapsed Time (T) for Various Core Sizes with Four Filaments

Core size	Steps	At the last step		
		N	T	s
0.10	142	2798	0.08937	97.46644
0.15	250	2113	0.31250	69.65556
0.20	250	1934	0.33125	66.26626
0.25	250	2264	0.435	81.34734
0.30	236	3314	0.5975	113.05148
0.40	250	2519	0.7075	84.75277
0.50	250	2451	1.25	72.87434
0.55	250	2257	1.25	67.20053
0.60	250	2219	1.29	66.05207

Note. These calculations were performed for four filaments using the fourth-order Runge–Kutta method and the core function 4 with the periodic data assumption and with parameters $t_0 = -0.2$, $C = 0.05$, $\Gamma = 5.0$, $\tau = 3.0$, and $\beta = 2.0$. The initial distance between filaments was 0.05.

TABLE VI

Comparisons of the Total Number of Computational Steps Performed, the Total Number of Segments (N) at the Last Computational Step, the Total Arclength (s) at the Last Computational Step, and the Elapsed Time (T) for Various Distances between Filaments

Distance between filaments	Core size = 0.2				Core size = 0.3			
	Steps	At last step			Steps	At last step		
		N	T	s		N	T	s
0.01	250	2295	2.015	78.917	172	3840	2.075	144.728
0.02	250	2009	1.800	68.281	205	3820	2.095	133.139
0.03	250	2054	1.605	70.700	233	3848	2.105	133.627
0.04	250	1981	1.425	68.079	218	3508	2.230	121.698
0.05	250	1934	1.325	66.266	237	3314	2.390	113.051
0.06	250	1928	1.275	64.977	242	3615	2.430	121.690
0.07	250	1956	1.265	64.943	250	3092	2.500	104.647
0.08	250	2027	1.255	67.644	250	2596	2.500	84.842
0.09	250	2361	1.255	79.363	250	2505	2.500	81.271
0.10	239	3337	1.195	110.628	250	2398	2.500	76.624
0.11	204	3425	1.020	115.288	250	2337	2.500	74.082
0.12	179	3196	0.895	109.033	250	2488	2.500	76.722
0.13	162	3118	0.810	107.001	229	3800	2.290	121.869
0.14	140	2955	0.700	103.022	195	3752	1.950	124.328
0.15	129	2802	0.645	124.123	198	3764	1.980	124.123

Note. These calculations were performed for four filaments using the fourth-order Runge–Kutta method and the core function 4 with the periodic data assumption and with parameters of core size $\sigma = 0.2$, $t_0 = -0.2$, $C = 0.05$, $\Gamma = 1.25$, $\tau = 3.0$, and $\beta = 2.0$.

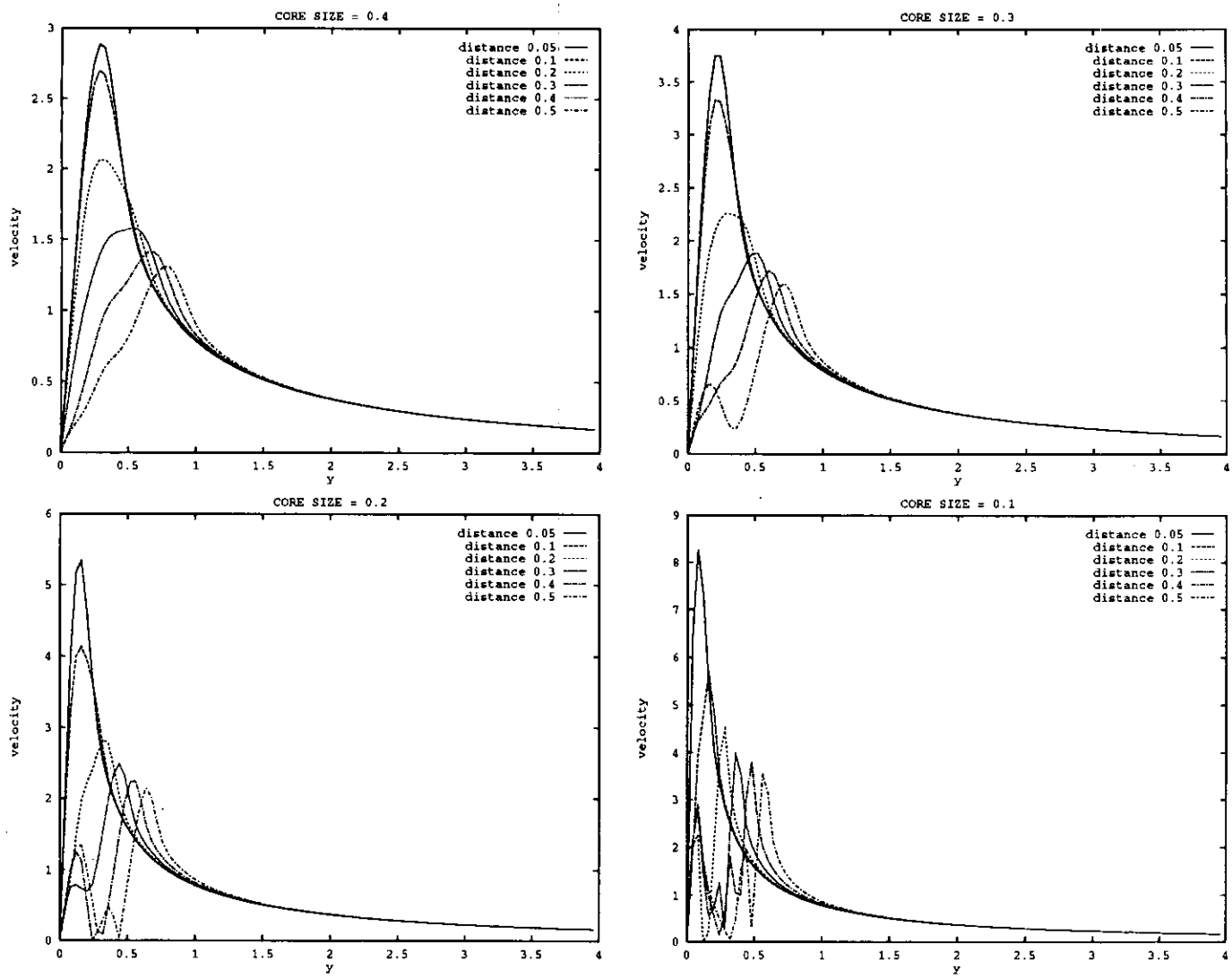

FIG. 3. Velocity distribution on a plane perpendicular to a straight vortex tube.

between filaments depends on the choice of core size. Figure 3 shows that if an initial distance between filaments is chosen to be greater than or equal to the core size, the induced velocity distribution will start to change its character. Figure 4 illustrates more clearly how velocity distribution changes when the distance between filaments is larger than core size σ.

Table VI shows that even with the initial distance between filaments less than the core size, the different choices of the distance will produce different results of stretching. The stretching rate will increase if the initial distance is larger than half of the core size. We therefore conjecture that the initial distance should not be larger than half of the core size.

To simulate a thin vortex tube, using several filaments with smaller initial distance between filaments will produce a result similar to the result obtained using one filament with other parameters unchanged. For each set of given parameters, there is a critical value for the initial distance between filaments at which the least stretching happens in the computational result. In Table VI, for core size $\sigma = 0.2$ the value is obtained around 0.06 and for core size $\sigma = 0.3$ the value is around 0.11. For core size $\sigma = 0.4$, which we did not provide full data in this paper, the value is around 0.10. Therefore, to avoid higher stretching in a numerical simulation of a vortex tube by a bundle of filaments, we may choose the distance between filaments close to the critical value. Note that vortex stretching could be physical. Therefore, it may not be reasonable to put our effort into eliminating all stretching. Besides there is no better method other than numerical experiment to find the cricial value. Because of the difficulty to determine the physical and numerical stretching, we are not able to give a precise method to choose the initial distance between filaments at this stage.

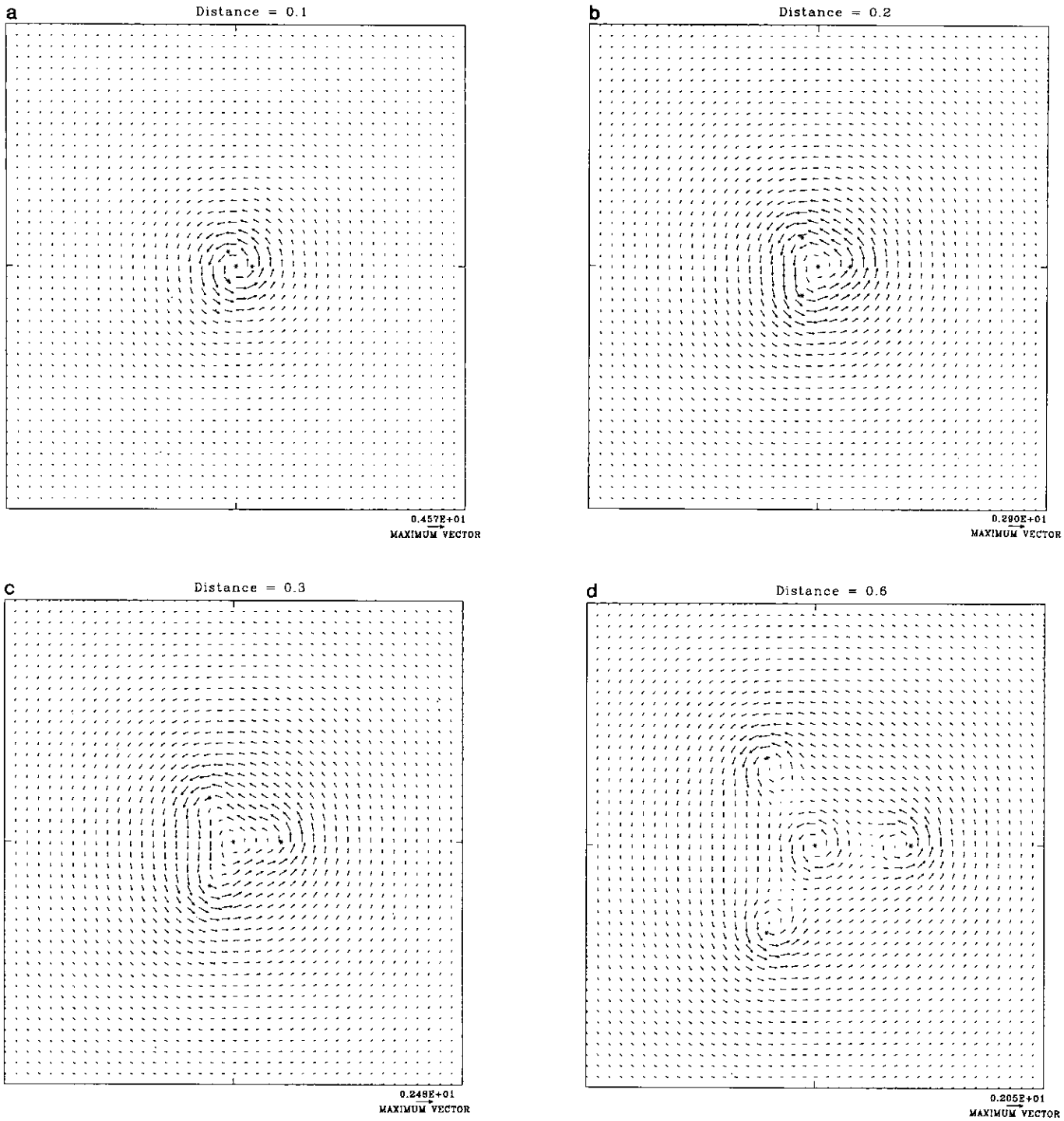

FIG. 4. Velocity fields induced by four filaments on cross section.

4.5. *The Torsion τ of the Initial Curve and Vortex Stretching*

The torsion τ of initial curve is clearly a physical factor. In Eq. (9), increasing $|\tau|$ will increase the speed and decrease the amplitude of the isolated helical wave contained in the initial curve. Geometrically, with smaller τ, a given curve will be closer to a plane curve. When $\tau = 0$, the given curve lies in a plane [30]. In our computation, we observed that when a vortex filament stretches, there is a part of the line whose curve is almost a plane curve; i.e., the curve has a small torsion. We consider this observation in this subsection and attempt to give an explanation.

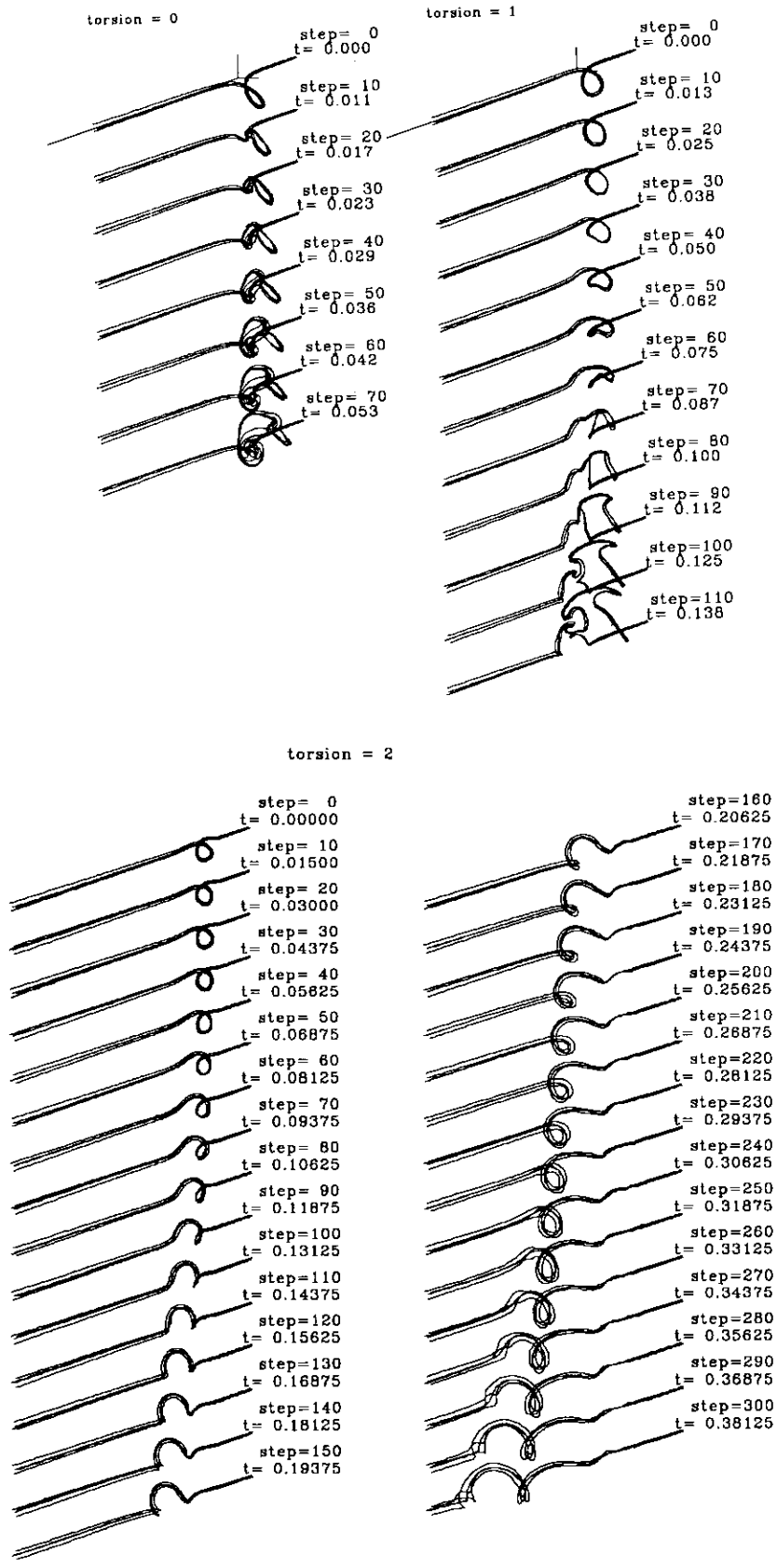

FIG. 5. Perspective views of wave propagating on four filaments for initial curves with various torsion τ.

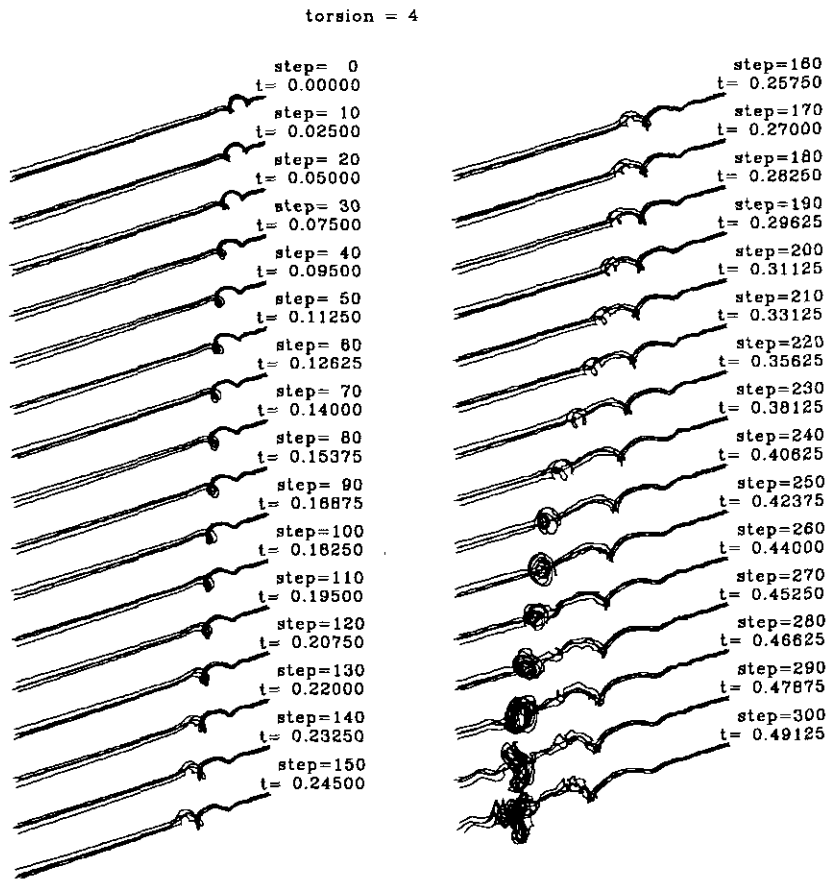

FIG. 5—*Continued*

Generating an initial curve, whose shape is determined by a constant torsion τ and the curvature, from the Hasimoto solitary wave solution of the LIA, we wish to see the effects of varying τ on the vortex stretching. The results are displayed in Table VII, which shows that vortex line stretching does not respond to the initial curve torsion τ monotonically. However, if τ is small enough, for example, in Table VII, if $\tau \leqslant 1.0$, the vortex stretching does occur directly on the initial wave, whereas if $\tau > 1.0$, waves with small torsion occur at where the stretching takes place. The occurrence of small torsion waves can be seen from the fact that the stretching is always highly concentrated on a narrow region along the x-axis on which the filament is lying. Curves confined in the narrow region on one direction are small torsion waves (Fig. 8).

Figure 5 gives the perspective views of wave propagating on four filaments with torsion $\tau = 0$, 1, 2, and 4, respectively, for the initial data. The choices of other parameters are given at Table VII. It can be seen clearly from Fig. 5 that the filaments are bent and wrap around the x-axis at where the original wave is located for $\tau \leqslant 1$. For $\tau = 2$, we obtained a long time propagation of the initial wave. For $\tau = 4$, the stretching occurred on a wave split from the main wave.

To understand the relation between vortex stretching and

TABLE VII

Comparisons of the Total Number of Computational Steps Performed, the Total Number of Segments (N) at the Last Computational Step, the Total Arclength (s) at the Last Computational Step, and the Elapsed Time (T) for Various Wave Torsion τ of Initial Data and for Both One Filament and Four Filaments Cases

	One filament				Four filaments			
	At the last step				At the last step			
τ	Step	N	T	s	Step	N	T	s
6.0	300	670	6.0000	16.15896	300	1950	0.75000	64.77505
5.0	300	647	6.0000	16.22601	300	1955	0.73125	64.38577
4.5	300	647	3.3400	17.03079	300	2605	0.60250	83.75597
4.0	234	988	2.4300	33.53885	300	2749	0.49125	92.79603
3.0	259	989	2.2200	34.90552	300	2335	0.39375	80.63711
2.5	300	512	2.6800	16.30441	300	2047	0.38625	70.28714
2.0	300	456	3.0000	16.23470	300	1860	0.38125	64.67449
1.0	90	968	0.5750	34.41537	118	3849	0.14750	136.68418
0.5	77	990	0.3925	34.96001	72	3677	0.09000	130.69027
0.0	67	992	0.2425	35.26452	70	3490	0.05313	125.24485

Note. These calculations were performed using the fourth-order Runge–Kutta method and the core function 4 with the periodic data assumption and with parameters of core size $\sigma = 0.2$ $t_0 = -0.2$, $C = 0.05$, $\Gamma = 5.0$, and $\beta = 2.0$. The initial distance between filaments was 0.05.

the torsion for the initial curve, we investigated the velocity field induced by the initial vortex curve generated from the Hasimoto solitary wave solution for the LIA with various values of torsion τ. Recall that each of the Hasimoto solitary wave curves has a constant torsion. Because of the difficulty to illustrate a three-dimensional velocity field on a two-dimensional paper, we plot two-dimensional slices of the velocity distributions from different angles instead.

In Fig. 6, we plot four slices of the velocity distributions on planes parallel to the plane $x = 0$. Each slice is taken at where the wave amplitude is a maximum. The geometrical center of each picture is where the x-axis passes through; that is, all filaments in each case rotate around the geometrical center of each picture. The "*" symbol in each picture indicates where the four filaments pass through the slice. We can see that if τ is smaller, the induced velocity will be dis-

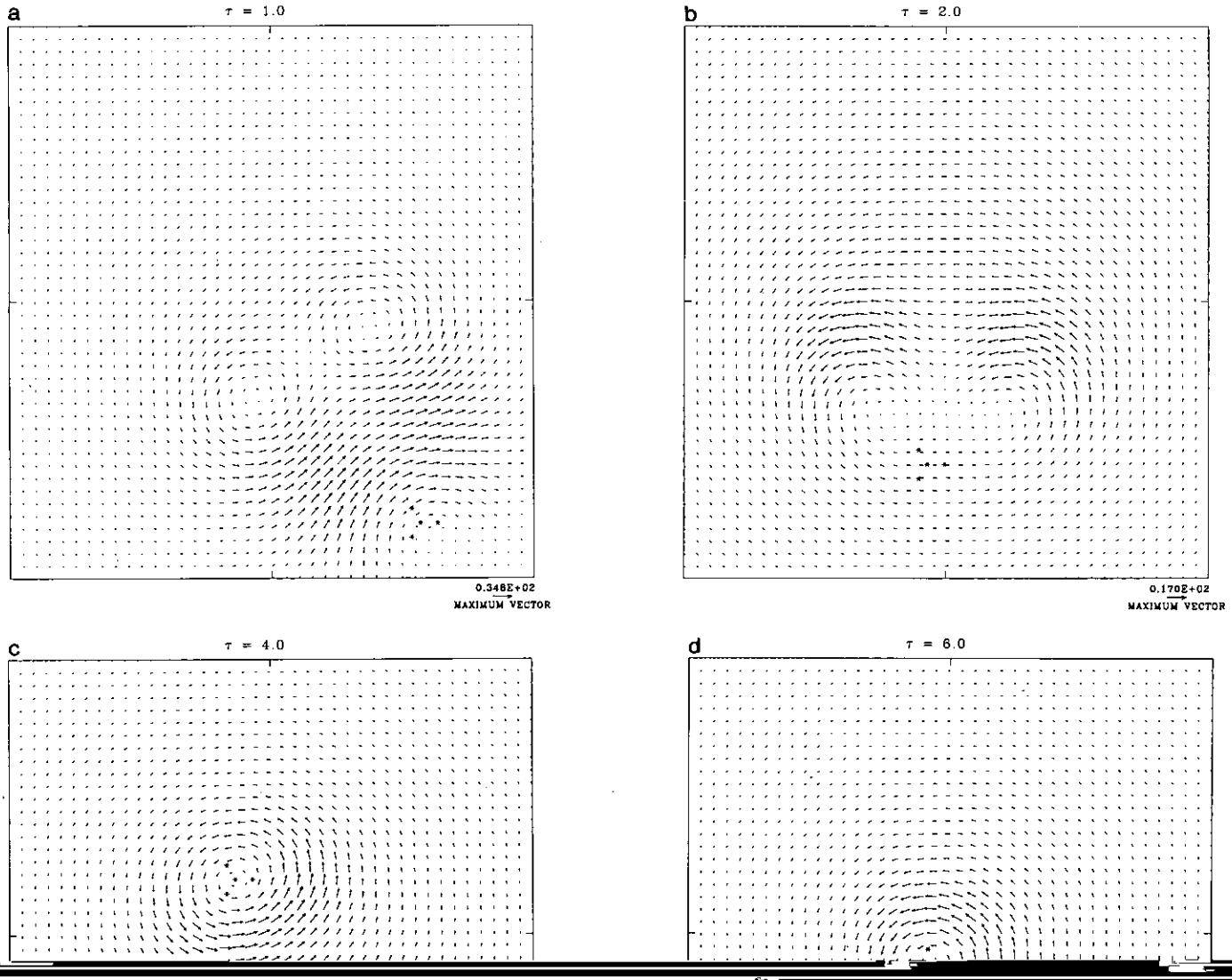

tributed in a more complicated pattern and less evenly on the slice through the peak of the wave. There is one pole for $\tau = 4$ and 6, two poles for $\tau = 2$, and a possible three poles for $\tau = 1$. It is very interesting to see that the velocity poles can stay away from the filaments in the cases $\tau = 2$ and $\tau = 1$. That is, for some cases, at certain slice of plane parallel to y-z plane, the velocity induced at that place is largely contributed by the parts away from a local region where the filaments exactly pass through. Such an induced velocity can only occur if the vortex line has small torsion curve. More complex the pattern of an induced velocity field is, more sensitive the vortex system is to the perturbation made in the vorticity field, thus more likely the violent stretching occur on the vortex lines.

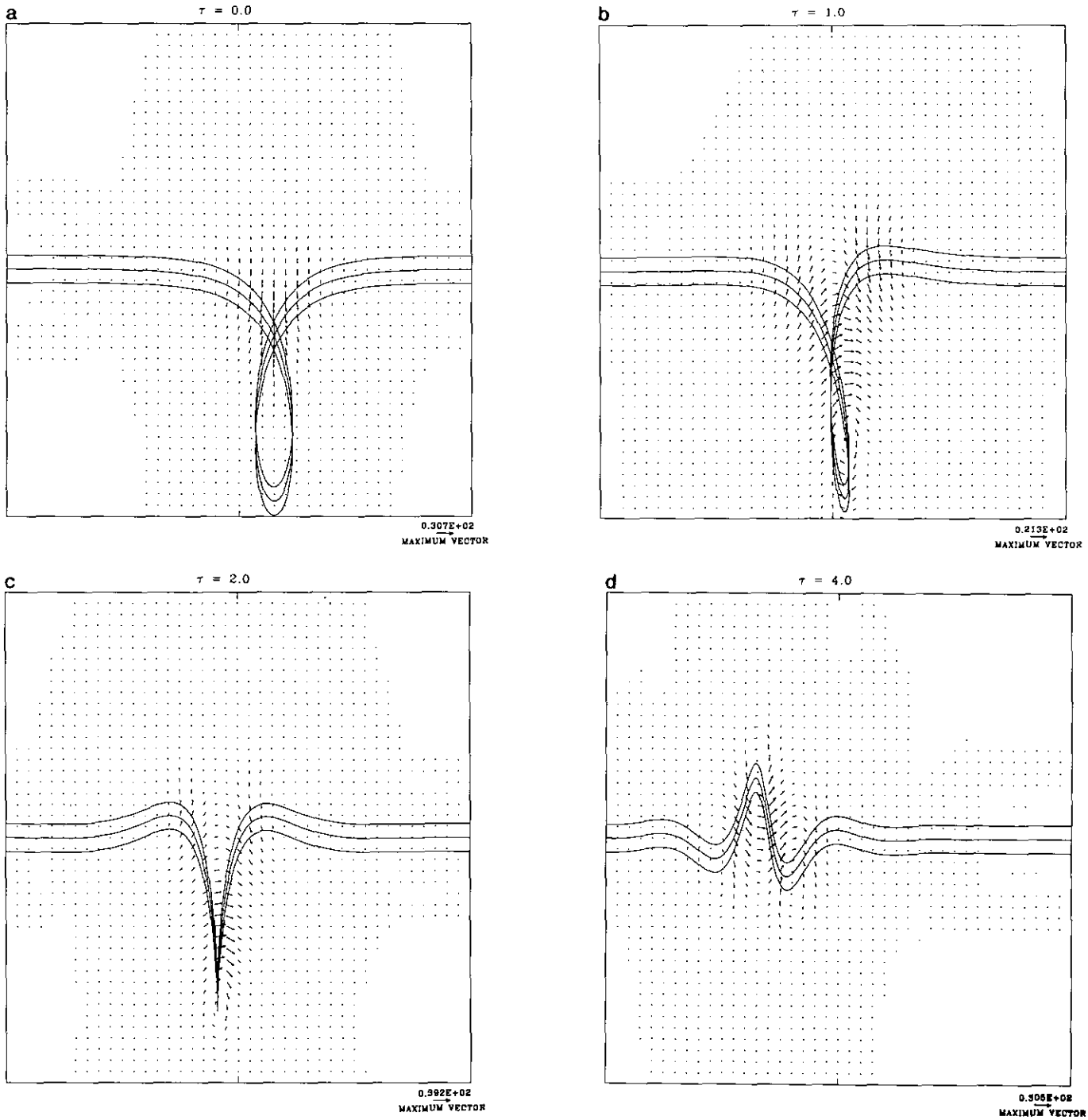

FIG. 7. Velocity distribution on the slice $y = 0$.

In Fig. 7, we plot the slices of the x-z plane, i.e., the plane in three-dimensional space with $y = 0$, of the velocity distributions for various values of τ. Let us look at a vertical line passing through the peak of the wave in each picture. On the line, in the cases $\tau = 2.0$ and $\tau = 4.0$, there are no significant alterations of the velocity vectors in the range the main wave reaches, whereas in the case $\tau = 1.0$, the velocity vectors near the wave peak is opposite to the velocity vectors in the rest part. Thus for the case $\tau = 1.0$, the vortex filaments are more likely bent and start to stretch, where the vortex lines possess maximum velocity intensity. For the case $\tau = 0$, the velocity distribution on the x-z plane is sym-

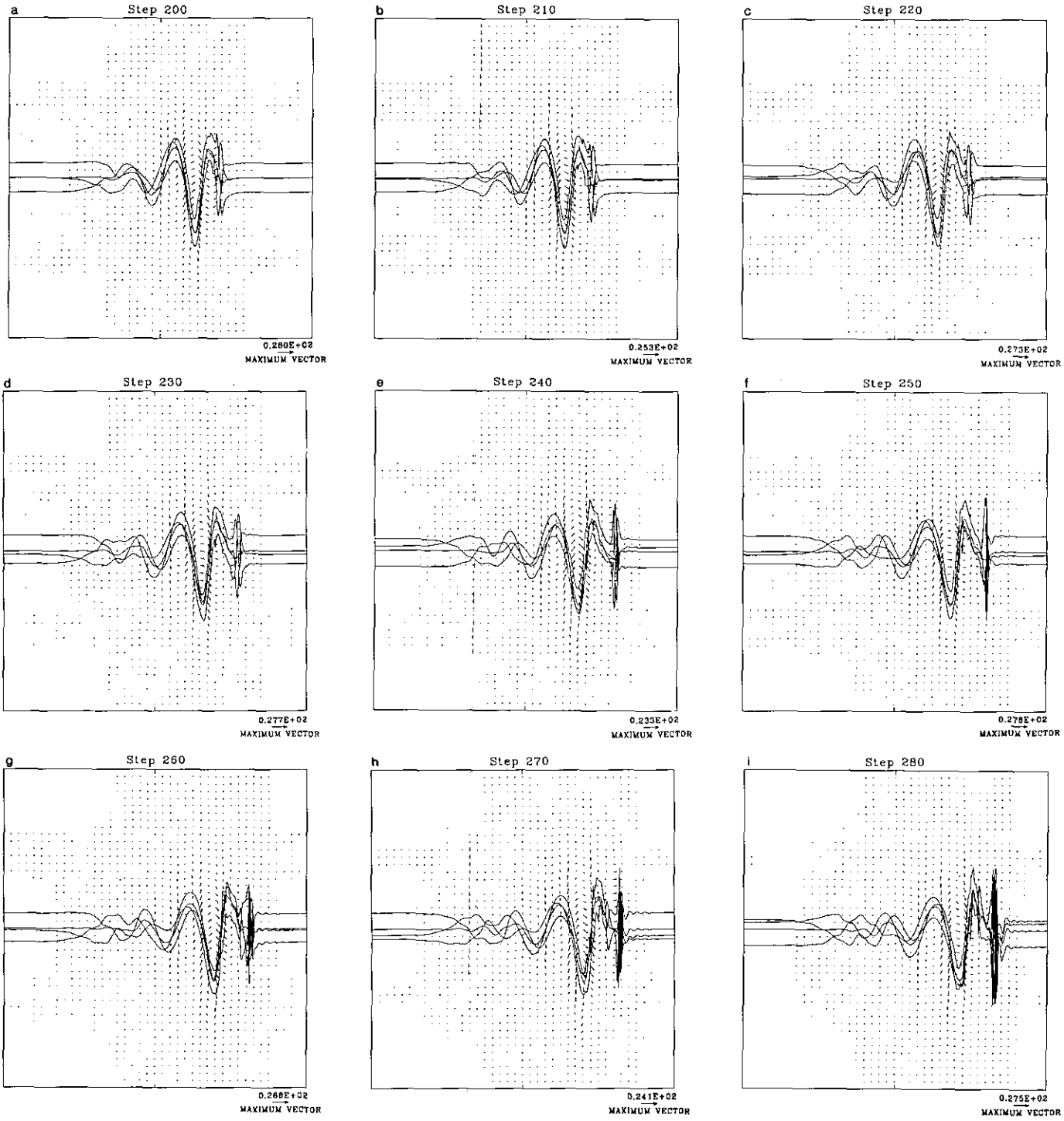

FIG. 8. Velocity distributions on the slice $y = 0$ and the evolution of vortex lines.

metric with respect to the vertical line passing through the peak of the wave. The velocity vectors are vertical on the line of symmetry. Thus the wave does not move along the x-axis; it instead stretches or is bent in the direction which the wave peak points.

We now consider the stretching that happens after the initial wave propagates for a while along a vortex tube. In Fig. 8 we plot the evolution of vortex lines projected on the x-z plane and their induced velocity distributions on the slice $y = 0$. The initial curve is generated from the Hasimoto solitary wave solution of the LIA with $\tau = 4.0$. The perspective view of the evolution of the vortex filaments is shown in Fig. 5. The nine pictures start from step 2000 and end at step 280, which illustrates the process of vortex stretching. One can see from step 200 to step 240 that, at the right front of the wave, the vortex lines become more vertical which means their torsion is small. The x-components of velocity vectors at the left side of the wave front are much larger than the ones at the right side. Such a distributed velocity field surely increases the vortex lines stretching because more wave lines are trapped at the right of wave front as the vortex filaments evolve and thus more complicated interactions between those lines will produce a further chaotic pattern of velocity field on a small scale, in particular, on the y- and z-components. The evidence is shown clearly in Fig. 8 from step 200 to step 280. The development of a violent stretching can be considered as the development of a singularity on a vorticity field.

4.6. *Summary and Discussion*

We have investigated eight factors listed in Subsection 4.1. Most questions we posed at the beginning of this section have been answered at this point. We summarize these answers here.

A. The higher-order numerical methods used to solve the time evolution ordinary differential equation generally give us more accurate results. The vortex tube simulation becomes more accurate as the number of filaments increases. The time tolerance control constant C is important to obtain an accurate result. Generally speaking, the smaller C we use, the higher accuracy we obtain, but the computation becomes more expensive. The core function is core size dependent. Core size too large or too small will produce inaccurate results. With core size in a reasonable range, presumably between 0.1 and 1 with single precision computation, the vortex filaments behave differently for various choices of core sizes. However, we are not able to determine the optimal core size analytically at present. The choice of the initial distance between filaments depends on the core size. The value of the initial distance should be less than half of the core size. But the optimal choice of the initial distance can only be determined by experiment and the nature of the simulated flow.

B. Core size and wave torsion are the two most sensitive factors in studying vortex stretching. A wave with small torsion on a vortex line more likely causes the vortex line stretching. The violent stretching part of a vortex line is confined in a narrow range at the propagating direction wave. We therefore think that a singularity is developed where a violent stretching happens.

Question C is equivalent to the question of whether a singularity in a vorticity field must occur in the evolution of a vortex tube. Recent results obtained with a newly developed numerical scheme shows that solitons do indeed exist on the vortex filaments with the velocity field induced by the Biot–Savart law [28]. Here, we illustrate a wave propagating in a periodic computing box and preserving its shape for a long time in Fig. 9. The computation is done with the method provided in this paper and with the periodic data assumption. The wave repeats in the periodic box once from step 0 to step 330. In the figure, we illustrated the wave before crossing the boundary of the periodic box at step 120 and the wave after crossing the boundary at step 180. At step 470, the wave is about to cross the boundary again. We computed a total 500 steps. The shape of the wave persists perfectly until the last step—the 500th step. Some authors also attempt to obtain better approximation of the Euler equations by improving the LIA [16]. The study of such improved approximation may provide an analytic answer to this question.

APPENDIX

Several invariants of the Euler equations are often used to check the validity of a numerical scheme for the Euler equations. They are the total vorticity Ω, linear impulse $\mathbf{I}$, and kinetic energy E of a vortex system, defined by

$$\Omega = \int \boldsymbol{\omega}\, dV \tag{21}$$

$$\mathbf{I} = \tfrac{1}{2}\int \mathbf{x} \times \boldsymbol{\omega}\, dV \tag{22}$$

$$E = \tfrac{1}{2}\int \mathbf{u} \cdot \mathbf{u}\, dV, \tag{23}$$

where we have assumed that the density is one.

For an unbounded flow with zero velocity and zero vorticity at infinity, for example, the closed ring, the total vorticity Ω is zero, and the kinetic energy and the linear impulse $\mathbf{I}$ are independent of time.

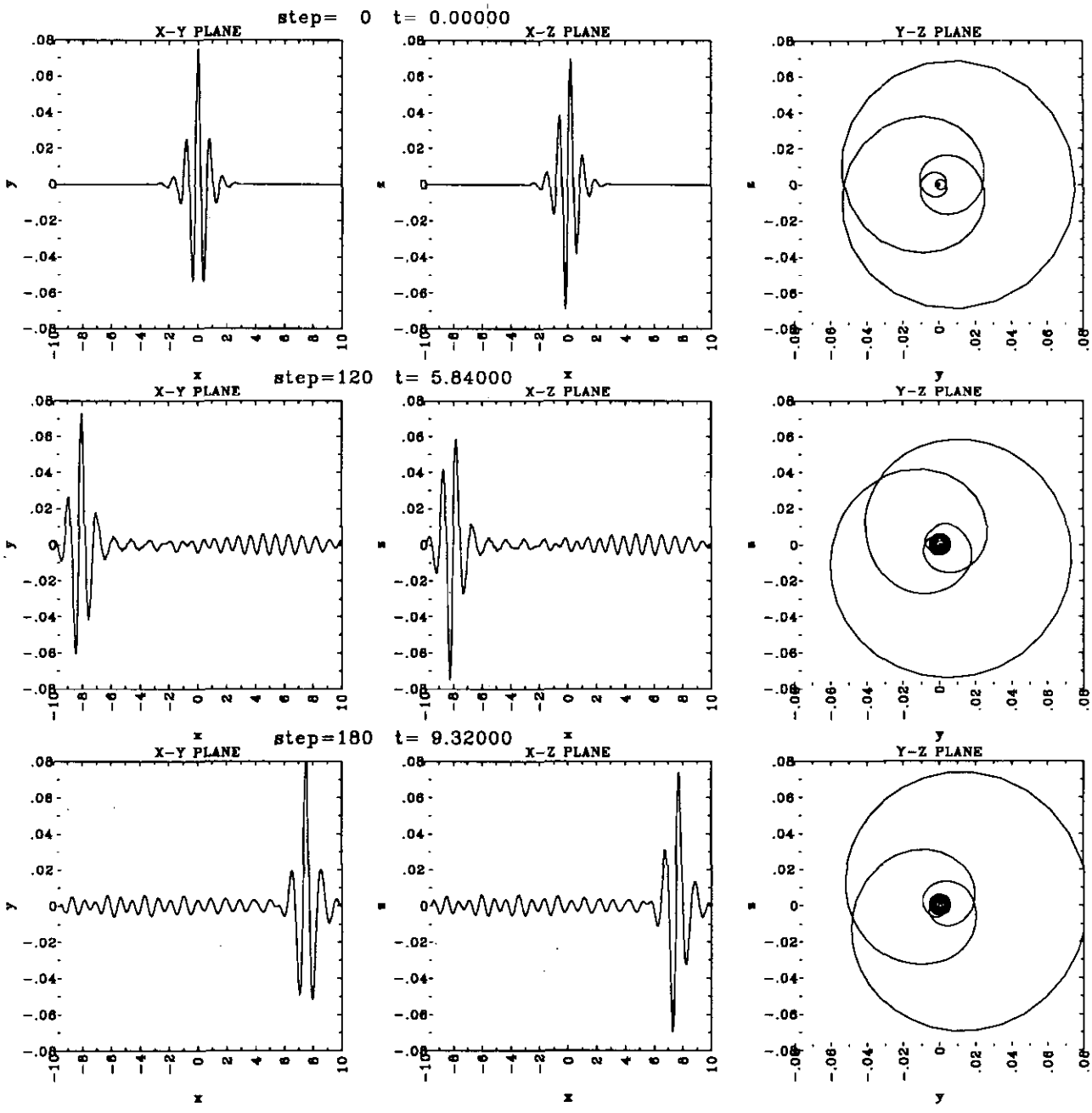

FIG. 9. A solitary wave propagation.

On the whole R^3 space, we can write the total kinetic energy as

$$E=\frac{1}{8\pi}\int_{R^3}\int_{R^3}\frac{\boldsymbol{\omega}\cdot\boldsymbol{\omega}'}{r}\,dV(\mathbf{x})\,dV(\mathbf{x}'). \tag{24}$$

This expression is the *Lamb integral* [20].

We call the conserved quantities such as kinetic energy, linear impulse, and total vorticity the diagnostics of a numerical scheme because a good numerical scheme for solving the Euler equation in an unbounded region should preserve these quantities. The discretizations of these diagnostics are based on the analysis used to obtain the vortex filament methods in Section 2,

$$\Omega\approx\sum_{m=1}^{M}\Gamma^{(m)}\sum_{j=-\infty}^{\infty}\delta\mathbf{l}_j^{(m)} \tag{25}$$

$$\mathbf{I}\approx\tfrac{1}{2}\sum_{m=1}^{M}\Gamma^{(m)}\sum_{j=-\infty}^{\infty}\mathbf{a}_j^{(m)}\times\delta\mathbf{l}_j^{(m)}, \tag{26}$$

where $\mathbf{a}_j^{(m)}=(\mathbf{x}_{j+1}^{(m)}+\mathbf{x}_j^{(m)})/2$.

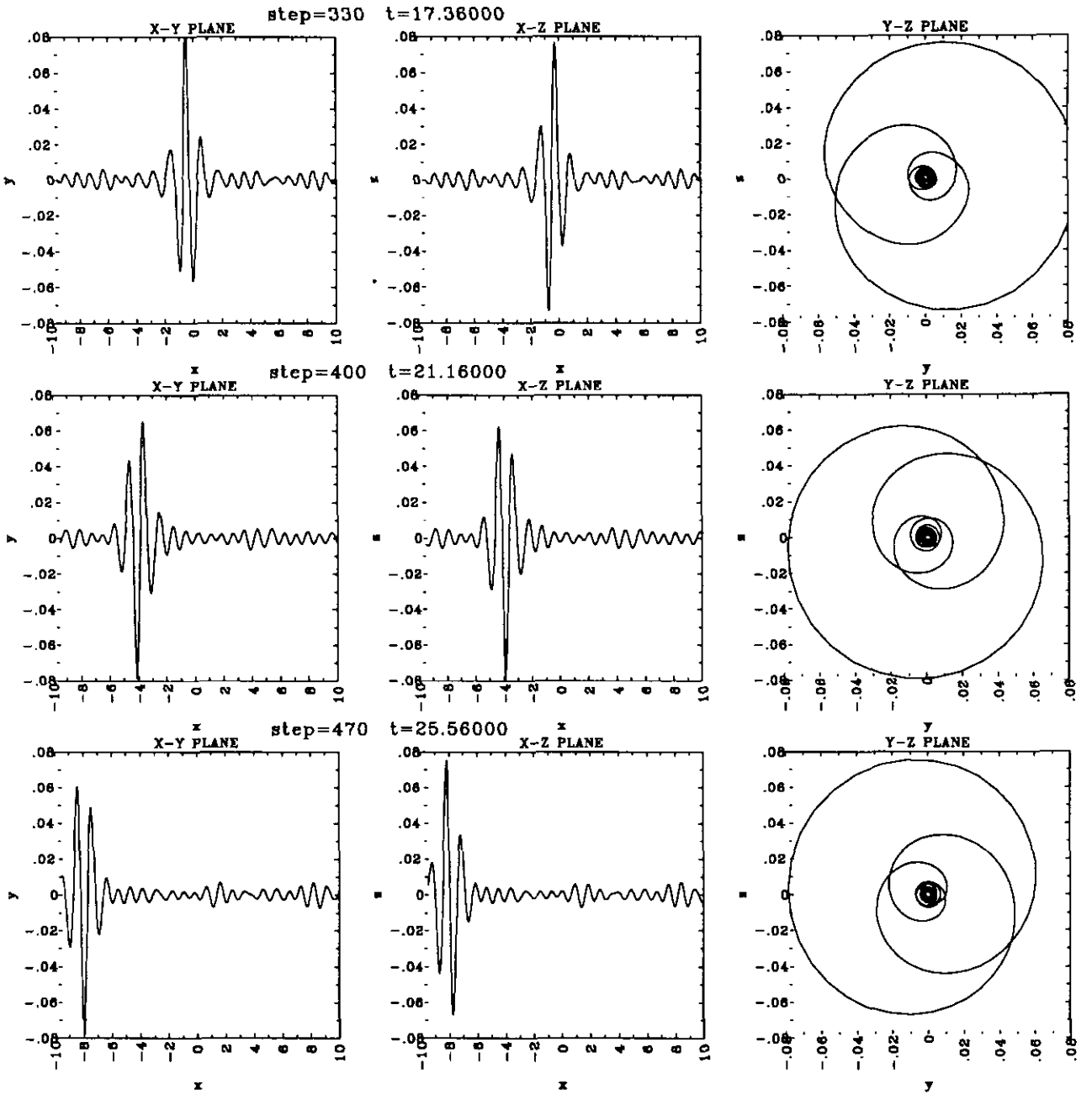

FIG. 9—*Continued*

The energy computation is a little more complicated. From Eq. (24),

$$E=\frac{1}{8\pi}\int_V\int_V \frac{\boldsymbol{\omega}(\mathbf{x})\cdot\boldsymbol{\omega}(\mathbf{x}')}{|\mathbf{x}-\mathbf{x}'|}\,dV(\mathbf{x})\,dV(\mathbf{x}')$$

$$=\frac{1}{8\pi}\sum_{i=-\infty}^{\infty}\sum_{j=-\infty}^{\infty}\int_{\delta V_i}\int_{\delta V_j}\frac{\boldsymbol{\omega}(\mathbf{x})\cdot\boldsymbol{\omega}(\mathbf{x}')}{|\mathbf{x}-\mathbf{x}'|}\,dV(\mathbf{x})\,dV(\mathbf{x}')$$

$$=\sum_{i=-\infty}^{\infty}\sum_{j\neq i}E_{ij}+\sum_{i=-\infty}^{\infty}E_{ii}, \tag{27}$$

where

$$E_{ij}=\frac{1}{8\pi}\int_{\delta V_i}\int_{\delta V_j}\frac{\boldsymbol{\omega}(\mathbf{x})\cdot\boldsymbol{\omega}(\mathbf{x}')}{|\mathbf{x}-\mathbf{x}'|}\,dV(\mathbf{x})\,dV(\mathbf{x}').$$

The total kinetic energy in a region consists of two parts. One is the sum of the E_{ii}, the *self-energy*, denoted by E_s; the other consists of the remaining terms, the *exhange energy*, denoted by E_e.

For these terms E_{ij} in E_e, $i \neq j$, under the more restrictive condition:

$$\max(|\delta \mathbf{l}_i|, |\delta \mathbf{l}_j|) \ll r_{ij}$$

where r_{ij} is the distance between the midpoints of two segments $\delta \mathbf{l}_i$ and $\delta \mathbf{l}_j$, we may approximate E_{ij} as usual,

$$E_{ij} = \frac{\Gamma_i \Gamma_j}{8\pi} \int_{\delta \mathbf{l}_i} \int_{\delta \mathbf{l}_j} \frac{d\mathbf{l}_i \cdot d\mathbf{l}_j}{|\mathbf{x} - \mathbf{x}'|} \approx \frac{\Gamma_i \Gamma_j}{8\pi} \frac{\delta \mathbf{l}_i \cdot \delta \mathbf{l}_j}{r_{ij}}.$$

However, it is clear that the terms E_{ii} in E_s cannot be approximated so simply, and E_{ii} is also too large to be ignored. One can resolve this difficulty by using a scaling property of E_{ii} [7–10].

To derive the scaling property of self-energy, we consider a piece of a cylindrical vortex tube with height l and cross-section radius σ—the core size defined prior to Eq. (10)—lying on the coordinate system given by Fig. 10. We denote the total kinetic energy induced by this piece as $E(\sigma, l)$; i.e.,

$$\begin{aligned} E(\sigma, l) = \frac{1}{8\pi} \int_{-\sigma}^{\sigma} dy \int_{-\sqrt{\sigma^2 - y^2}}^{\sqrt{\sigma^2 - y^2}} dz \\ \times \int_0^l dx \int_{-\sigma}^{\sigma} dy' \int_{-\sqrt{\sigma^2 - y'^2}}^{\sqrt{\sigma^2 - y'^2}} dz' \\ \times \int_0^l dx' \frac{\boldsymbol{\omega}(\mathbf{x}) \cdot \boldsymbol{\omega}(\mathbf{x}')}{|\mathbf{x} - \mathbf{x}'|}. \end{aligned} \tag{28}$$

Clearly, the vorticity $\boldsymbol{\omega}$ depends on the radius σ and can be written as $\boldsymbol{\omega}_\sigma = (\xi_\sigma, 0, 0)$ in the given coordinate system. We will assume that the circulation $\boldsymbol{\omega}_\sigma \cdot \mathbf{n} A(\sigma) = \xi_\sigma A(\sigma)$ is fixed, where $A(\sigma) = \pi\sigma^2$; that is, for a real parameter $\varepsilon > 0$,

$$\xi_{\varepsilon\sigma}(\varepsilon \mathbf{x})\, A(\varepsilon\sigma) = \xi_\sigma(\mathbf{x})\, A(\sigma)$$

or

$$\xi_{\varepsilon\sigma}(\varepsilon \mathbf{x}) = \frac{1}{\varepsilon^2} \xi_\sigma(\mathbf{x}). \tag{29}$$

A simple computation [27] shows that

$$E(\varepsilon\sigma, \varepsilon l) = \varepsilon E(\sigma, l).$$

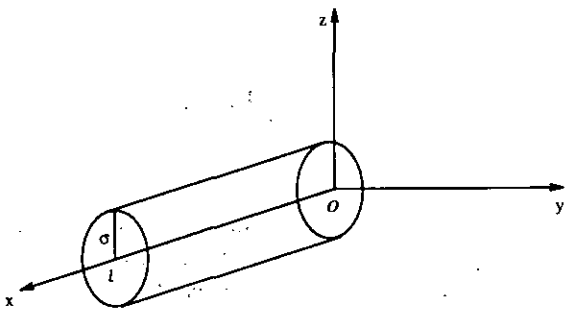

FIG. 10. A piece of a cylindrical vortex tube.

Let $\varepsilon = 1/\sigma$; we then find that

$$E(\sigma, l) = \sigma E(1, l/\sigma) = \sigma T(l/\sigma), \tag{30}$$

where $T(l) = E(1, l)$ is a single variable function.

With the assumption that the vorticity $\boldsymbol{\omega}_\sigma$ is constant in space and time, e.g., $\boldsymbol{\omega}_\sigma(\mathbf{x}) \cdot \boldsymbol{\omega}_\sigma(\mathbf{x}') = C(\sigma) \cdot T(l)$ has the asymptotical properties

$$T(l) \sim \text{const} \cdot l \ln l \qquad \text{for} \quad l \to +\infty$$

$$T(l) \sim \text{const} \cdot l^2 \qquad \text{for} \quad l \to 0$$

(see [27] for a detailed derivation).

Now we compute $T(l)$. Once we make a table of $T(l)$, we can use interpolation and Eq. (30) to compute $E(\sigma, l)$ for any given σ and l. Since the vorticity $\boldsymbol{\omega}$ depends on core structure, we should not assume $\boldsymbol{\omega}$ to be a constant vector. We must evaluate $T(l)$ from Eq. (28). Therefore we need to compute $\boldsymbol{\omega}_\sigma$ first. From Eq. (17) and (10) and the definition of $\psi_\sigma(\mathbf{x})$ Section 2, following part (iii),

$$\begin{aligned} \boldsymbol{\omega}_\sigma(\mathbf{x}, t) &= \frac{\Gamma}{4\pi} \int_{C_t} \frac{f'(r/\sigma)\, d\mathbf{l}(\mathbf{x}')}{\sigma r^2} \\ &= \frac{\Gamma}{4\pi\sigma} \sum_{j=-\infty}^{\infty} \int_{\delta \mathbf{l}_j} \frac{f'(r/\sigma)\, d\mathbf{l}(\mathbf{x}')}{r^2} \\ &\approx \frac{\Gamma}{4\pi\sigma} \sum_{j=-\infty}^{\infty} \frac{f'(a_j/\sigma)\, \delta \mathbf{l}_j}{a_j^2}, \end{aligned} \tag{31}$$

where $r = |\mathbf{x} - \mathbf{x}'|$ and $a_j^2 = |(\mathbf{x}_{j+1} + \mathbf{x}_j)/2 - \mathbf{x}|^2$. From the first equality, we can see that

$$\boldsymbol{\omega}_{\varepsilon\sigma}(\varepsilon \mathbf{x}, t) = \frac{1}{\varepsilon^2} \boldsymbol{\omega}_\sigma(\mathbf{x}, t)$$

which justifies the assumption of Eq. (29). From Eq. (31),

$$\begin{aligned} T(l) \approx \frac{\Gamma^2}{128\pi^3} \int_0^{2\pi} d\theta \int_0^1 d\rho \int_0^l dz \\ \times \int_0^{2\pi} d\theta' \int_0^1 d\rho' \int_0^l dz' \\ \times \frac{\rho\rho' \sum_{i=-\infty}^{\infty} \sum_{j=-\infty}^{\infty} (f'(a_i) f'(a_j')\, \delta \mathbf{l}_i\, \delta \mathbf{l}_j / a_i^2 a_j'^2)}{\sqrt{\rho^2 + \rho'^2 - 2\rho\rho' \cos(\theta - \theta') + (z - z')^2}} \end{aligned}$$

which can be evaluated by standard integration schemes. The self-energy can be computed as

$$E_s = \sum_{i=-\infty}^{\infty} \sigma_i T(l_i/\sigma_i), \tag{32}$$

where $l_i = |\delta \mathbf{l}_i|$. The total kinetic energy is given by the approximate expression

$$E = E_e + E_s,$$

where $E_s = \sum_{i=-\infty}^{\infty} \sum_{j \neq i} E_{ij}$, $E_{ij} = (\Gamma_i \Gamma_j / 8\pi)(\delta \mathbf{l}_i \, \delta \mathbf{l}_j / r_{ij})$ and E_s is given by Eq. (32).

One must be cautious for the use of these numerical schemes of the diagnostics. On a finite part of an unbounded vorticity field, the linear impulse may not be conserved; the total kinetic energy of this part may not be expressed as Eq. (24). Therefore when we compute a finite part of an unbounded vorticity field, the linear impulse of this part should not be used as a diagnostic quantity, and the numerical scheme (27) may not provide correct answers for the total kinetic energy of this part.

To demonstrate our point, let us consider an infinitely long vortex tube lying on x-axis, i.e., the center line of the tube approaches the x-axis for an x component that is large enough. Let us pick up a portion of the tube with the volume of the portion defined as

$$W_t = \{(x, y, z) : a(t) \leqslant x \leqslant b(t), \ -\infty < y, z < +\infty\},$$

where subscript t means the volume moving with the flow.

It is clear that the total vorticity in the given portion W_t does not vanish. However, the total vorticity in the given portion W_t is independent of time,

$$\begin{aligned} \frac{d}{dt} \int_{W_t} \boldsymbol{\omega} \, dV &= \frac{d}{dt} \int_{W_t} \nabla \times \mathbf{u} \, dV \\ &= \int_{W_t} \nabla \times \frac{D\mathbf{u}}{Dt} \, dV \\ &= -\int_{W_t} \nabla \times (\nabla P) \, dV = 0, \end{aligned}$$

where we have used the Euler equations (1) and (2).

Generally, in the restricted region W_t, the kinetic energy is not conserved, and Eq. (24) is not equivalent to Eq. (23), due to the nonvanishing boundary terms. We denote $\mathbf{u} = (u, v, w)^t$, $\boldsymbol{\omega} = (\xi, \zeta, \gamma)^t$, and $\boldsymbol{\Psi} = (\psi_1, \psi_2, \psi_3)^t$. Let us compute dE/dt on W_t,

$$\begin{aligned} \frac{dE}{dt} &= \int_{W_t} \frac{D}{Dt} (\mathbf{u} \cdot \mathbf{u}) \, dV \\ &= \frac{1}{2} \int_{W_t} \mathbf{u} \cdot \frac{D\mathbf{u}}{Dt} \, dV \\ &= -\frac{1}{2} \int_{W_t} \mathbf{u} \cdot \nabla P \, dV \\ &= -\frac{1}{2} \int_{W_t} \nabla (\mathbf{u} P) \, dV \\ &= -\frac{1}{2} \int_{\mathbf{R}^2} [(uP)|_{x=a}^{x=b}] \, dA(y, z), \end{aligned}$$

where we used the fact that

$$\mathbf{u} \cdot \nabla P = \nabla (\mathbf{u} P) - (\nabla \cdot \mathbf{u}) P = \nabla (\mathbf{u} P)$$

since $\nabla \cdot \mathbf{u} = 0$. The last surface integration does not vanish unless $\mathbf{u} = 0$ or $P = 0$ at both planes $x = a$ and $x = b$. Therefore the kinetic energy E in the restricted region W_t is not conserved generally.

On the other hand, the kinetic energy E can be expressed as

$$E = \tfrac{1}{2} \int \boldsymbol{\Psi} \cdot \boldsymbol{\omega} \, dV - \tfrac{1}{2} \int \nabla \cdot (\mathbf{u} \times \boldsymbol{\Psi}) \, dV.$$

The second term cannot be eliminated generally on the restricted portion W_t because

$$\int_{W_t} \nabla \cdot (\mathbf{u} \times \boldsymbol{\Psi}) = \int_{\mathbf{R}^2} [(v\psi_3 - w\psi_2)|_{x=a}^{x=b}] \, dA(y, z).$$

Thus, on the restricted portion W_t, Eq. (24) is not equivalent to Eq. (23) generally.

The linear impulse in the restricted region W_t is also not conserved generally. Let us compute $d\mathbf{I}/dt$,

$$\frac{d\mathbf{I}}{dt} = \int_{W_t} \frac{D}{Dt} (\mathbf{x} \times \boldsymbol{\omega}) \, dV = \int_{W_t} \left(\mathbf{u} \times \boldsymbol{\omega} + \mathbf{x} \times \frac{D\boldsymbol{\omega}}{Dt} \right) dV,$$

where

$$\begin{aligned} &\int_{W_t} \mathbf{u} \times \boldsymbol{\omega} \, dV \\ &= \int_{W_t} \left[\frac{1}{2} \nabla (\mathbf{u} \cdot \mathbf{u}) - \frac{\partial (u\mathbf{u})}{\partial x} - \frac{\partial (v\mathbf{u})}{\partial y} - \frac{\partial (w\mathbf{u})}{\partial z} \right] dV \\ &= \begin{pmatrix} \frac{1}{2} \int_{\mathbf{R}^2} [(v^2 + w^2 - u^2)|_{x=a}^{x=b}] \, dA(y, z) \\ -\int_{\mathbf{R}^2} [(uv)|_{x=a}^{x=b}] \, dA(y, z) \\ -\int_{\mathbf{R}^2} [(uw)|_{x=a}^{x=b}] \, dA(y, z) \end{pmatrix} \end{aligned}$$

and

$$\int_{W_t} \mathbf{x} \times \frac{D\boldsymbol{\omega}}{Dt} \, dV = \int_{W_t} \mathbf{x} \times (\boldsymbol{\omega} \cdot \nabla) \mathbf{u} \, dV.$$

Both the surface integration and the integration $\int_{W_t} \mathbf{x} \times (\boldsymbol{\omega} \cdot \nabla) \mathbf{u} \, dV$ do not vanish generally. Therefore, $d\mathbf{I}/dt \neq 0$; that is, the linear impulse in the restricted region W_t is not conserved.

ACKNOWLEDGMENTS

I thank Professor A. Chorin and Professor O. Hald for many helpful

16. R. Klein and A. J. Majda, *Physica D* **49**, 323 (1991).
17. O. M. Knio and A. F. Ghoniem, *J. Comput. Math. Phys.* **86**, 75 (1988).
18. P. Krasny, *J. Comput. Phys.* **65**, 292 (1986).